Three-dimensional Multi-site Random Access Photostimulation (3D-MAP)

Yi Xue[1], Laura Waller[1], Hillel Adesnik[2,*], and Nicolas Pégard[3,4,5,‡]

[1]Department of Electrical Engineering & Computer Sciences, University of California, Berkeley, CA, USA
[2]Department of Molecular & Cell Biology, University of California, Berkeley, CA, USA
[3]Department of Applied Physical Sciences, University of North Carolina at Chapel Hill, NC, USA
[4]Department of Biomedical Engineering, University of North Carolina at Chapel Hill, NC, USA
[5]UNC Neuroscience Center, University of North Carolina at Chapel Hill, NC, USA
Corresponding authors: *hadesnik@berkeley.edu, ‡pegard@unc.edu

Abstract

Optical control of neural ensemble activity is crucial for understanding brain function and disease, yet no technology can achieve optogenetic control of very large numbers of neurons at extremely fast rate over a large volume. State-of-the-art multiphoton holographic optogenetics requires high power illumination that only addresses relatively small populations of neurons in parallel. Conversely, one-photon holographic techniques can stimulate more neurons with 2-3 orders lower power, but with a trade-off between resolution and addressable volume. Perhaps most problematically, two-photon holographic optogenetic systems are extremely expensive and sophisticated which has precluded their broader adoption in the neuroscience community. To address this technical gap, we introduce a new one-photon light sculpting technique, Three-Dimensional Multi-site random Access Photostimulation (3D-MAP), that overcomes these limitations by modulating light dynamically, both in the spatial and in the angular domain at multi-kHz rates. We use 3D-MAP to interrogate neural circuits in 3D and demonstrate simultaneous photostimulation and imaging of dozens of user-selected neurons in the intact mouse brain *in vivo* with high spatiotemporal resolution. 3D-MAP could be broadly adopted for high-throughput all-optical interrogation of brain circuits owing to its powerful combination of scale, speed, simplicity, and cost.

1

Introduction

Optogenetics enables rapid and reversible control of neural activity[1,2]. By focusing light on neurons[3] with either one-photon[4-12] or two-photon photostimulation[13-24], one can elicit or suppress the activity of custom neural ensembles in order to map neural circuits[8,9,14-16] and draw links between specific patterns of neural activity and behavior[6,7,10,13,20-22]. Two-photon photostimulation has the advantages of high spatial resolution for precise neural activity control and relative immunity to tissue light scattering, enabling precise stimulation of deep brain circuits. However, two-photon holographic optogenetic photostimulation can only stimulate relatively small ensembles of neurons at a time, limited by the very high-power pulsed illumination required to achieve non-linear multiphoton absorption. High photon density heats brain tissue, and can disturb brain activity and cause thermal damage[24,25]. The accessible volume for holographic two-photon photostimulation is also limited by the coherence length of laser being used, since holographic diffraction of femtosecond pulses to a large angle introduces severe pulse dispersion ('chirp'), substantially reducing pulse peak power[26]. Mechanically scanning a single focus or a holographic pattern can access a larger volume, but at the expense of simultaneous illumination[27] which is important to understand the network. But perhaps the primary barrier for their broader adoption is that multiphoton optogenetic systems are extremely expensive and sophisticated to operate and to maintain and thus, despite more than a decade since their introduction, have only been adopted by a small handful of groups, typically with much prior optical expertise.

2

49 In contrast, one-photon photostimulation systems require two to three orders-of-

50 magnitude less laser power to activate neurons. They are much simpler to implement with

51 far less expensive hardware, and they can still achieve high resolution photostimulation

52 under limited light scattering conditions. There are three main strategies to generate

53 multiple foci with one-photon photostimulation, yet none is capable of simultaneously

54 stimulating specific multiple neural ensembles over a large 3D volume with high spatial

55 resolution. The first approach, scanning-based one-photon photostimulation, stimulates

56 neurons sequentially by rapidly scanning a single focus across small neural clusters with

57 scanning mirrors[28] or acousto-optic deflectors (AODs)[29,30]. This method cannot photo-

58 stimulate distributed ensembles simultaneously. The second approach is to directly

59 project 2D illumination patterns onto samples with a Digital Micromirror Device (DMD)[8-12].

60 This widefield illumination scheme has a large field-of-view (FOV) and moderate lateral

61 resolution but only modulates light in 2D. The axial resolution is poor and yields unwanted

62 photostimulation above and below the focal plane. The third approach, Computer

63 Generated Holography (CGH), generates 3D distributed foci by phase modulation of

64 coherent light in Fourier space using a spatial light modulator (SLM)[4-7]. One-photon CGH

65 has high lateral resolution and moderate axial resolution but has several critical

66 drawbacks that constrain its ability to execute sophisticated optogenetics experiments.

67 First, the throughput of CGH that determines the number of accessible voxels is

68 fundamentally limited by the number of degrees-of-freedom (DoF), which is determined

69 by the number of pixels and the bit depth of the SLM, regardless of magnification and

70 numerical aperture. This generally results in a relatively small FOV at high spatial

71 resolution. Second, the refresh rate (tens to hundreds Hz) of SLMs limits the speed of

3

72   CGH. Third, CGH requires computing a 2D phase mask at the Fourier plane for a 3D

73   hologram pattern, which is an ill-posed problem that requires iterative optimization, with

74   computation time on the order of minutes[31-34] when shaping light across multiple z-planes.

75   Although recent work successfully reduces the CGH computation time to milliseconds

76   using a pre-trained deep neural network[35], the computation time could be very long when

77   the neural networks become larger as the number of z-planes increases. The extra

78   computational requirements for generating holographic patterns in the Fourier domain

79   (rather than directly projecting patterns on the conjugate image plane) can become

80   limiting when thousands of different patterns are required (as in high throughput mapping

81   experiments), or when fast online synthesis of custom patterns is needed for closed-loop

82   experiments. The fourth drawback of one-photon CGH is that holograms composed of

83   many illumination spots will suffer spatial cross-talk as out-of-focus light from each

84   focused spot interacts, accidentally stimulating non-targeted neurons. Taken together,

85   despite the power of these previous one-photon techniques, none are suitable for large-

86   scale high resolution optogenetic activation of 3D distributed ensembles of neurons.

87

88   To overcome this challenge, we developed 3D multi-site random access photostimulation

89   (3D-MAP), a new approach to generate 3D illumination patterns by modulating light both

90   in the angular domain, (k_x, k_y), with scanning mirrors and in the spatial domain, (x, y),

91   with a DMD. For 3D optogenetic photostimulation, illumination patterns must be optimized

92   to target an opsin expressed neuronal soma (~10μm). The set of light rays needed to

93   generate each spherical target can be described with a 4D light field, (x, y, k_x, k_y), in the

94   spatio-angular domain. 3D-MAP generates these rays by rapidly sweeping through the

4

95 appropriate angles of illumination with scanning mirrors while projecting the

96 corresponding amplitude masks with the DMD to pattern each angle's spatial information.

97 3D-MAP uses one spatial pattern on the DMD for each unique illumination angle set by

98 the scanning mirrors. The total number of DoF is hence determined by the *product* of the

99 number of angles of the scanning mirror and the pixels of the DMD (as opposed to the

100 sum), resulting in a much larger DoF than existing one-photon optogenetic stimulation

101 techniques[4-12]. Thus, 3D-MAP achieves both high spatial resolution and a large

102 accessible volume. Compared to one-photon CGH, 3D-MAP is able to reduce spatial

103 cross-talk by prioritizing illumination angles that minimize the stimulation of non-targeted

104 areas due to its high DoF. Compared to 2D widefield patterning methods, 3D-MAP retains

105 the advantages of high throughput and computational efficiency, while extending the

106 addressable space from 2D to 3D. Thanks to the use of a DMD instead of a SLM, we can

107 pattern the entire addressable volume at multi-kHz rate (the volumetric pattern refresh

108 rate), which exceeds the bandwidth of most neural circuits and is one order-of-magnitude

109 faster than 3D CGH. For reference, a comparison between strengths and weaknesses of

110 3D-MAP versus existing photostimulation approaches is shown in Supplementary Table

111 1.

112

113 We present the experimental setup and computational methods for all-optical

114 interrogation of neural circuits in 3D, and we demonstrate that 3D-MAP achieves high

115 resolution, high speed, and high throughput in brain slices and *in vivo* recorded by

116 electrophysiology and optical detectors, respectively. We then use 3D-MAP to interrogate

117 neural circuits with both single-spot photostimulation and multi-spot photostimulation in

118   3D. These experiments validate 3D-MAP as a one-photon technique to manipulate neural

119   circuits on-demand with high spatiotemporal resolution in the intact brain. Our technique

120   can be flexibly used to map neural connectivity at both small and large scales. Its relative

121   simplicity, small hardware footprint, and lower cost should make it broadly adoptable

122   across the neuroscience community, and thus facilitate all-optical interrogation of neural

123   circuits and behavior in the future.

124
125   **Results**

126   ***Optical Design of 3D-MAP***

127   The experimental setup for 3D-MAP is shown in Figure 1. A DMD modulates amplitude

128   in real space, (x, y), while scanning mirrors control the angles of illumination, (k_x, k_y).

129   Both devices are placed at conjugate image planes (Figure 1A) and time-synchronized

130   (see Materials and Methods for details). We first compute the desired intensity of the light

131   field (x, y, k_x, k_y), and then sequentially display the amplitude mask pattern on the DMD

132   as the scanning mirrors sweep through the relevant angles (Figure 1B). For example, in

133   the simplest case of patterning a single focus spot at the native focal plane (z=0), we

134   simply turn on the pixels corresponding to the desired position, keeping the pattern

135   constant for all illumination angles. To create a focused spot at an off-focus plane, a small

136   aperture on the DMD rotates in a circle as the scanning mirrors sweep through a cone of

137   projection angles (Figure 1B). The center of the aperture's revolving circle is the lateral

138   position of the target spot, and the circle's diameter, D, determines the spot's axial

139   position (a larger diameter concentrates light further away from the native image plane at

140   an given illumination angle). To activate multiple neurons simultaneously, we simply

141   superimpose the patterns corresponding to each target (Figure 1D). In addition, we can

       6

142 adjust the laser power in each focused spot flexibly and individually by adjusting the

143 aperture size on the DMD, the number of apertures aimed at a given target, and by

144 adjusting the laser power if needed. The amount of light on any given target is

145 quadratically proportional to the radius of the aperture. For example, changing the

146 aperture radius from 10 pixels to 14 pixels will increase the stimulation power on the target

147 by a factor 2 times.

148

149 Another way to describe the pattern design is that the amplitude masks are computed by

150 tracing the perspective views of the target back to the objective's native focal plane along

151 parallel ray directions set by the scanning mirrors. Hence, even complicated 3D target

152 designs can be computed quickly and easily. In contrast, conventional CGH systems

153 synthesize a 3D hologram by modulating a coherent laser beam with a 2D static phase

154 mask at the conjugate Fourier plane, which is an ill-posed problem where the 3D pattern

155 is an approximate solution. CGH uses coherent light that introduces speckle in the

156 hologram pattern (Figure 1C, Figure 1—figure supplement 1A-D), and out-of-focus light

157 above and below each targeted area generates cross-talk that unintentional activates

158 non-targeted neurons. Conversely, 3D-MAP modulates light incoherently in time which

159 eliminates speckle. The cross-talk can be reduced simply by not selecting certain

160 illumination angles to avoid stimulating non-targeted areas, further enhancing the

161 stimulation accuracy and efficiency (Figure 1C). More strategies to reduce cross-talk are

162 discussed in the Discussion section.

163

164 The axial resolution of 3D-MAP depends on the number of beams (and their angles) that

165 are sequentially projected to generate the targeted 3D intensity pattern (Figure 1E-F).

166 Because the fastest frame refresh rate of the DMD (13kHz, or 77μs per frame) is about

167 52-fold shorter than the stimulation time (4ms, see later sections for details), we can use

168 up to 52 angles without sacrificing speed. However, the DMD has limited on-chip memory,

169 so we choose to minimize the number of amplitude masks required. In all our

170 experiments, we use 10 illumination angles for each 3D target; additional illumination

171 angles only introduce minor improvements of the axial resolution (Figure 1E-F). The

172 maximum refresh rate of the DMD is 13kHz, and each 3D volumetric pattern is generated

173 by 10 masks on the DMD, so the maximum volumetric pattern rate is 1.3kHz, which is

174 more than an order-of-magnitude faster than conventional CGH with commercial SLMs.

175 Since the characteristic response time of the microbial opsin is much longer than the

176 duration of individual projection masks, the relevant light sculpting pattern seen by the

177 opsin is the time-averaged sum of the intensity of several mutually incoherent masks. In

178 addition, the DMD masks for 3D-MAP are based on ray tracing and can be calculated

179 much faster than phase holograms in CGH[31-34], enabling real-time applications such as

180 mapping neural circuits (see below).

8
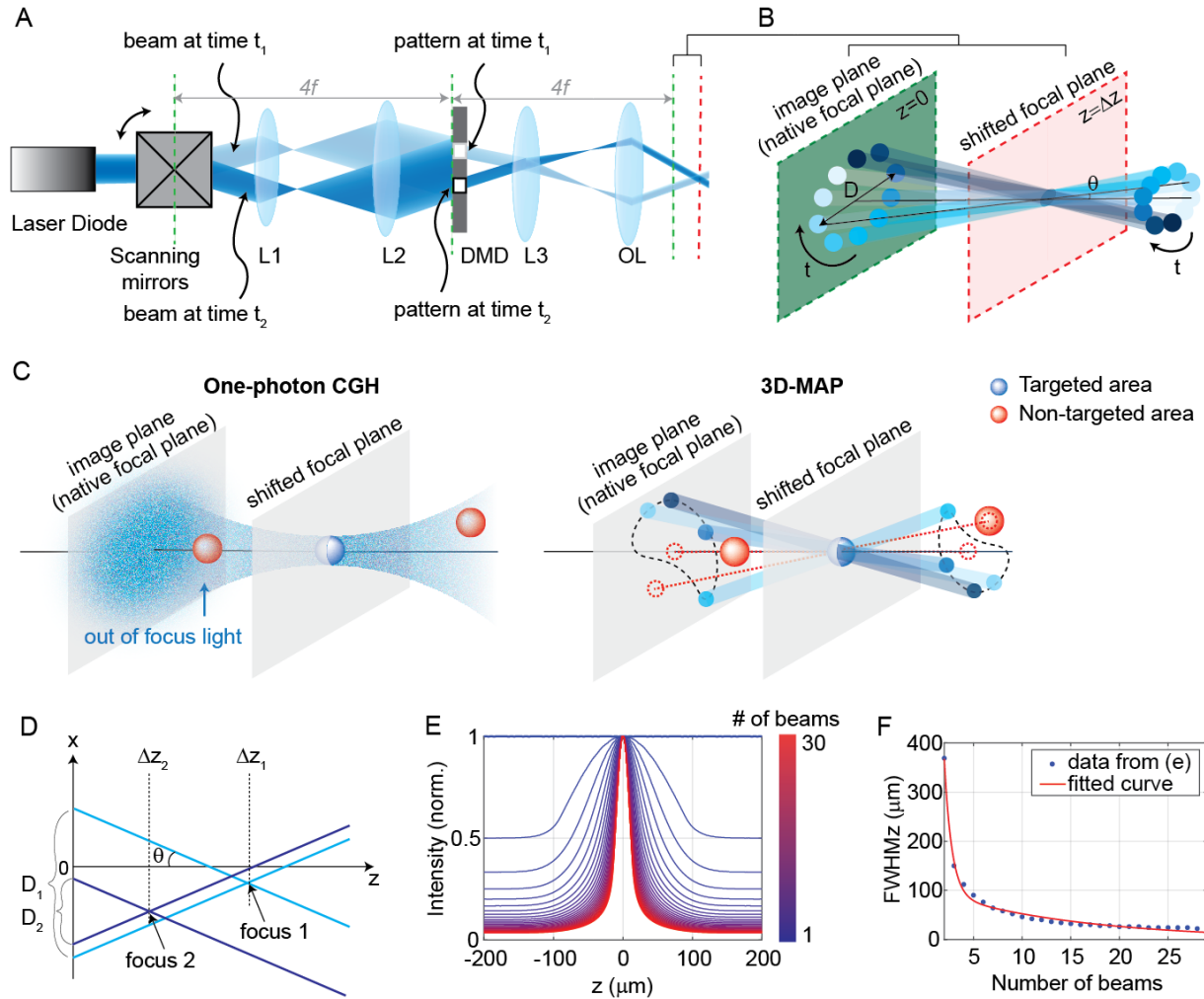
Figure 1. Experimental setup for Three-dimensional random Access Photostimulation (3D-MAP). (A) A collimated laser beam illuminates the surface of a DMD with a custom illumination angle set by scanning mirrors. The DMD is synchronized with the scanning mirrors to match the 2D mask of the spatial aperture to the illumination angle. (B) Detailed view of the overlapping amplitude masks and illumination angles at the conjugate image plane (green) showing how synchronized illumination angles and amplitude masks can generate a focused spot away from the native focal plane (red). Circular patterns labeled by different colors are spatial apertures projected at different times. The position illuminated by all beams while sweeping through each illumination angle forms a focus at the shifted focal plane at $z=\Delta z$. D is the diameter of the sweeping trace. θ is the illumination angle. (C) A focus generated by CGH stimulates the targeted area (blue) in focus but also stimulates non-targeted areas (red) out of focus. 3D-MAP can stimulate only the targeted areas and avoid non-targeted areas by closing the amplitude apertures along propagation directions that project to non-targeted areas (dashed red line). (D) Multiple foci can be generated simultaneously at various depths by superposition of their perspective projection along each illumination angle. (E) Simulated maximum intensity profile along the z-axis for an increasing number of overlapping beams shows how axial resolution increases with the number of superimposed projection directions. (F) Full width at half maximums (FWHMs) of the illumination patterns in (E). The data for a single beam is excluded because it has no z-sectioning ability.

9

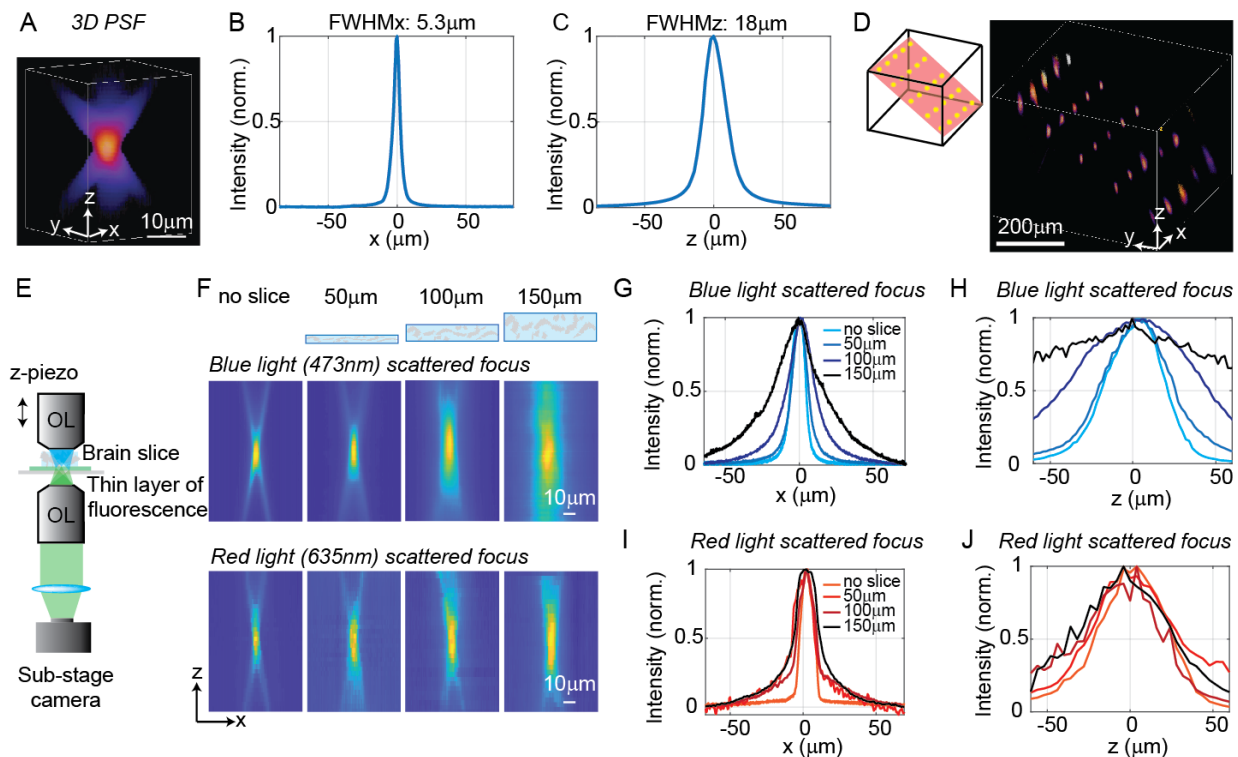### *Optical Characterization of 3D-MAP*

202 To quantify the optical resolution of 3D-MAP, we first measured the 3D optical point-

203 spread-function (PSF). We turned on a one-pixel aperture on the DMD (acting as a point

204 source) and scanned through angles by scanning mirrors to generate a focus, which is

205 imaged by a sub-stage camera with a thin fluorescent film on a microscope slide at many

206 depth planes (Figure 2A-C). The full-width-half-maximums (FWHMs) of the resulting 3D

207 optical PSF indicate a spatial resolution of 5x5x18µm^3 with a 473nm excitation

208 wavelength. We also demonstrated the ability to simultaneously generate 25 foci at

209 custom (x, y, z) locations in a 744x744x400 µm^3 volume (Figure 2D). Additional examples

210 of simultaneous 3D multi-spot generation are shown in Figure 2—figure supplement 1A-

211 B. The foci on the edge of the accessible volume are slightly larger than the foci in the

212 center generated by the same size aperture (63% larger along the x-axis and 38% larger

213 along the z-axis on average for foci that are 300µm away from the center, Figure 2—

214 figure supplement 1C-J). Together, these data show that 3D-MAP achieves high spatial

215 resolution for multi-site stimulation over a large volume.

216

217 We next quantified the effects of optical scattering in mouse brain tissue on focusing

218 capabilities with 3D-MAP by measuring the size of a target after propagating through

219 acute brain slices (brain slices that are kept vital *in vitro* for hours) of increasing thickness

220 placed just above the thin fluorescent film (Figure 2E). We generated a focused target by

221 turning on a 10-pixel radius aperture on the DMD (8µm in diameter at the native focal

222 plane) to produce an illumination volume matching the typical dimensions of a neuronal

223 soma in the cortex. We note that this target size is larger than the spatial resolution limit

10

224 of 3D-MAP, but that it represents a practical choice of 3D pattern that matches the size

225 of neurons and our application. We compared scattering for both blue (473nm) and red

226 (635nm) excitation wavelengths. Without the brain slice, the size of the focus was

227 $11.7 \times 11.7 \times 42\mu m^3$ (473nm blue) and $10.4 \times 10.4 \times 50.7\mu m^3$ (635nm red). When generating

228 the focus through 50μm, 100μm and 150μm thick brain slices, the size of the focus spot

229 with blue light increased by 8%, 75%, and 269%, and the size of the focus spot with red

230 light increased by 67%, 107%, and 114%, respectively (averaged values measured along

231 the x-axis and the z-axis). Compared to other one-photon photostimulation techniques[6,12],

232 3D-MAP achieves high optical resolution especially when the scattering is weak (in brain

233 slices or in superficial layers *in vivo*), and the resolution can be improved in the future by

234 using red stimulation light combined with red-shifted opsins such as Chrimson or

235 ChRmine (see Discussion).

236

237

11

238 **Figure 2. Optical characterization of the spatial resolution of 3D-MAP under increasing optical**
239 **scattering conditions.** (A) Experimentally measured 3D optical PSF (1-pixel aperture on DMD) built from
240 focus-stacked 2D images of a thin, uniform fluorescent calibration slide recorded at different depths using
241 a sub-stage camera. (B) The PSF's lateral cross-section (x-axis) has a FWHM of 5.3μm. (C) The PSF axial
242 cross-section (z-axis) has a FWHM of 18μm. (D) Left: we simultaneously generated 25 foci spanning across
243 a 744x744x400μm^3 volume. Right, experimental measurement of the corresponding 3D fluorescence
244 distribution. (E) Schematic diagram of the sub-stage microscope assembly for 3D pattern measurement.
245 (F) XZ cross-section of the PSF, measured with blue (473nm) and red (635nm) light stimulation without
246 scattering, and through brain tissue slices of increasing thickness: 50μm, 100μm, and 150μm. (G) Under
247 blue light illumination, the FWHM along the x-axis for increasing amounts of scattering is 11.7μm, 12.2μm,
248 19.7μm, and 29.0μm, and (H) the FWHM along the z-axis is respectively 42μm, 46μm, 76μm and 122μm.
249 (I) With red light illumination, the FWHM along the x-axis for increased amounts of scattering is 10.4μm,
250 19.3μm, 26.7μm, and 29.6μm, and (J) the FWHM along the z-axis is respectively 50.7μm, 75.4μm, 79.7μm,
251 and 73.1μm.
252
253

254 ### *3D-MAP Photostimulation in brain tissue*

255 We next quantified the physiological spatial resolution as measured by the physiological

256 point spread function (PPSF) of 3D-MAP by stimulating neurons in acute mouse brain

257 slices and *in vivo*. We performed whole-cell patch clamp recordings from L2/3 excitatory

258 neurons expressing a soma-targeted version of the potent optogenetic protein ChroME[24]

259 (see Materials and Methods). The PPSF measures the photocurrent response as a

260 function of the radial and axial displacements between the targeted focus and the patched

261 cell[19]. The physiological spatial resolution is not only related to the optical PSF but also

262 to the laser power needed to a drive a neuron to spike[36]. Since patterns for 3D-MAP can

263 be calculated significantly faster than with CGH[31-34], we measured the volumetric PPSF

264 by recording the photocurrent response from 2,541 targeted locations (a 11x11x21 pixels

265 grid) in 2-5 minutes, limited only by opsin kinetics. We chose a 4ms stimulation time (also

266 known as 'dwell time') in all experiments to ensure full activation of opsins (Figure 3—

267 figure supplement 1), followed by 8ms to 40ms inter-stimulation time (time between two

268 stimulation pulses in successive targets, depending on the opsin type) to avoid

269 photocurrent accumulation and minimize short term plasticity of the synapses under study.

12

270   Note that this is a specific choice for our experiments rather than the speed limit of 3D-

271   MAP. The PPSF measurements show that 3D-MAP provides high resolution

272   photostimulation *in vitro* (lateral FWHM, 29±0.8µm; axial FWHM, 44±1.6µm, 9 cells,

273   Figure 3A-D). Under these conditions, we found that the spatial specificity of 3D-MAP is

274   only approximately two-fold worse when compared to our previous results using

275   multiphoton optogenetics in comparable conditions[19,24]. We note that the PPSF of

276   photocurrents for 3D-MAP should degrade more steeply as a function of tissue depth

277   compared to multiphoton optogenetics due to scatter (see details in Discussion).

278

279   To quantify the physiological resolution of 3D-MAP for supra-threshold neuronal

280   activation, we also measured the spiking probability of neurons in acute brain slices and

281   *in vivo* along the lateral and axial dimensions. We targeted opsin-expressing neurons in

282   the upper 100µm of the brain for the *in vivo* PPSF measurements. While patching the

283   neuron, we digitally displaced the target generated by 3D-MAP along the x-axis and z-

284   axis and record the number of spikes. Experimental results show that 3D-MAP enables

285   high spatial specificity under all these conditions (Figure 3E-G shows *in vitro* results (5

286   cells), with lateral FWHM, 16±2.4µm; and axial FWHM, 44±8.9µm. Figure 3H-J shows *in*

287   *vivo* results (8 cells), with lateral FWHM, 19±3.7µm; and axial FWHM, 45±6.1µm).

13

288

289
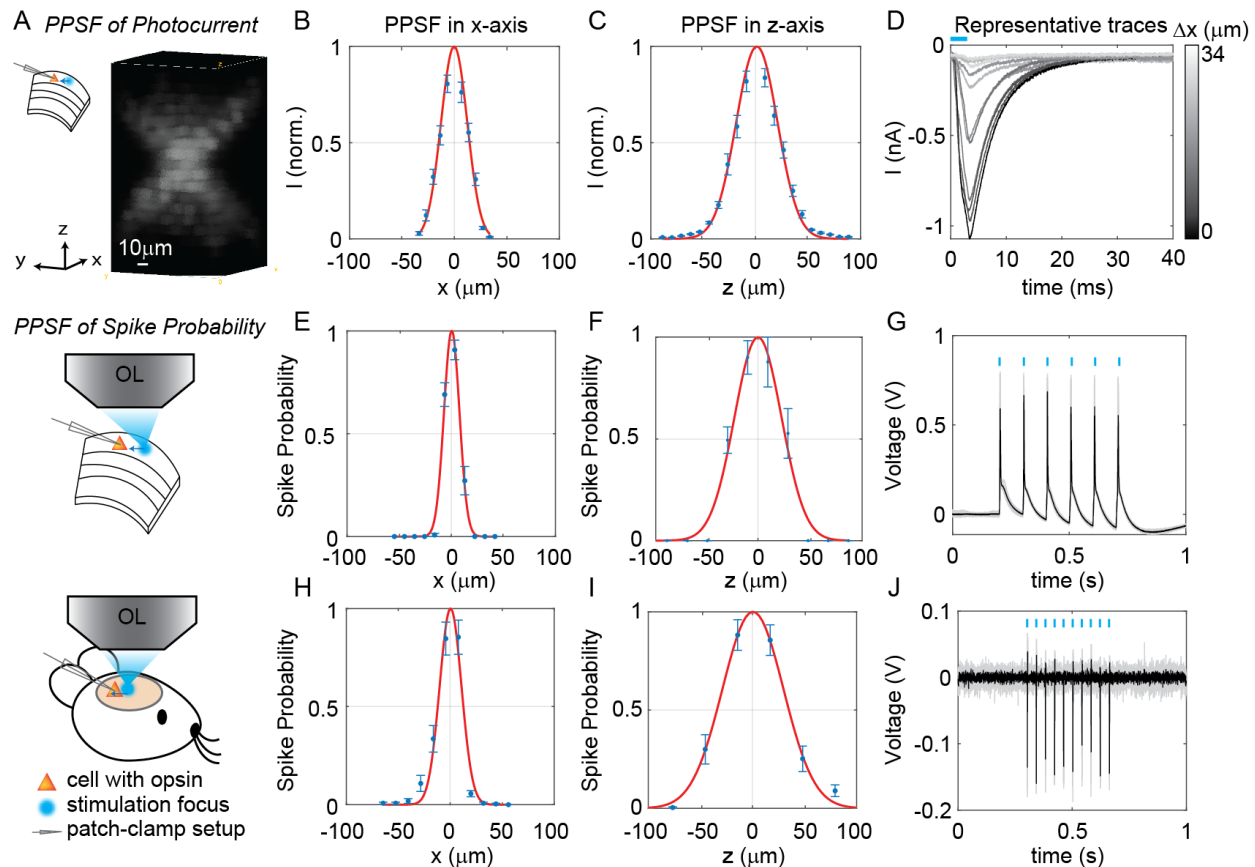
Figure 3. 3D-MAP enables high spatial resolution photo-activation of neurons *in vitro* and *in vivo*. (A) Example 3D representation of a physiological point spread function (PPSF) photocurrent measurement *in vitro*. (B, C) Photocurrent resolution (FWHM) is 29±0.8µm laterally, and 44±1.6µm axially (n=9 neurons). (D) Representative traces of direct photocurrent from 11 positions along the x-axis without averaging. (E, F) 3D-MAP evoked spiking resolution in brain slices is 16±2.4µm laterally and 44±8.9µm axially (n=5 neurons). (G) Representative traces of spike probability of 1 for *in vitro* measurements. (H, I) 3D-MAP evoked spiking resolution measured *in vivo* is 19±3.7µm laterally and 45±6.1µm axially (n=8 neurons). (J) Representative traces of spike probability of 1 for *in vivo* measurements. The data shows the mean ± s.e.m. (standard error of the mean) for plots B-C, D-F, and H-I.

299

Synaptic connectivity mapping over large volumes by a single focus

In addition to high spatiotemporal resolution and fast computational speed, 3D-MAP operates at low stimulation powers far below photodamage thresholds and is hence easily sca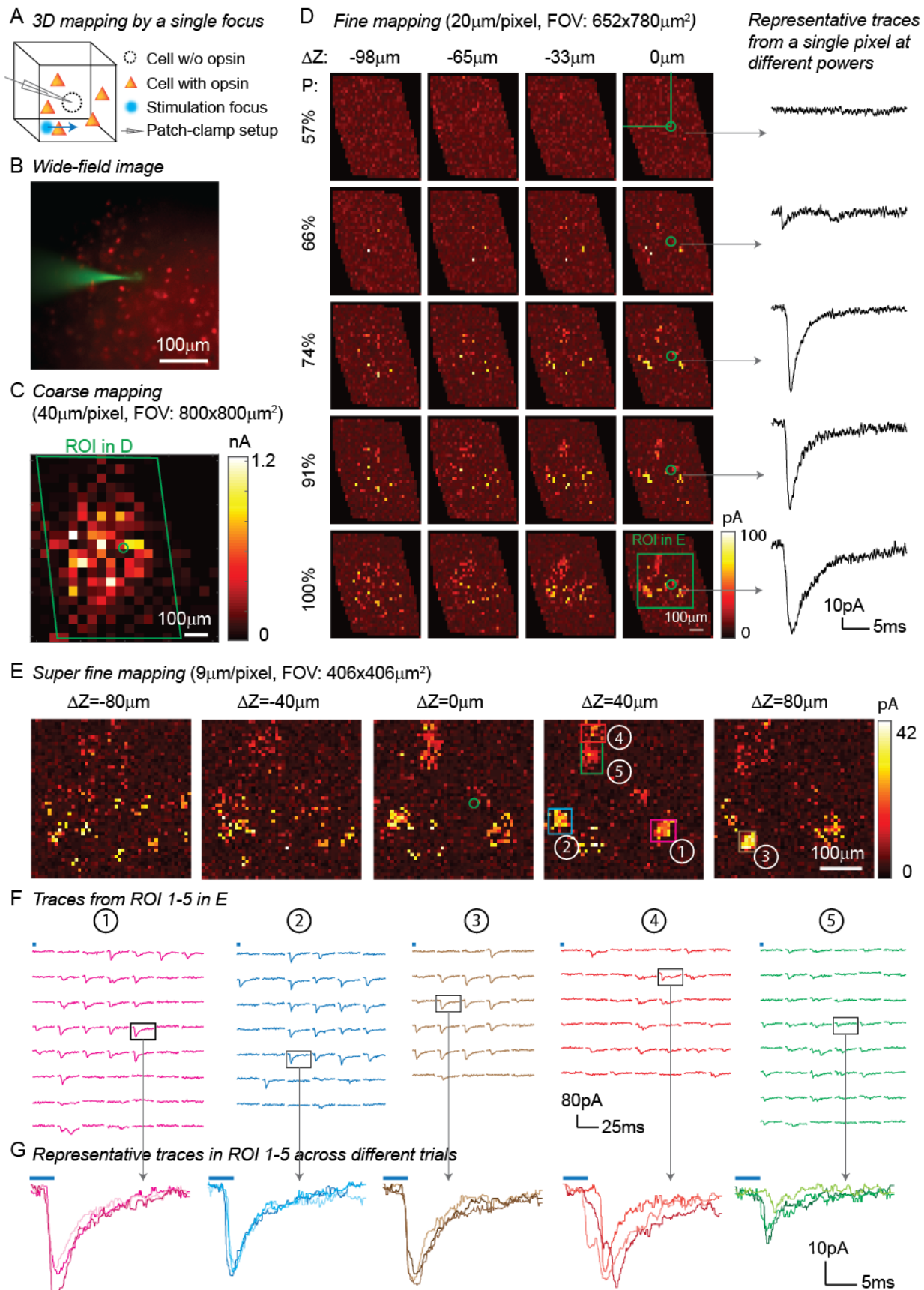lable to address large neural ensembles in distributed volumes of brain tissue. To demonstrate these advantages, we first used 3D-MAP to probe synaptic connectivity in 3D by randomly scanning a single focus (Figure 4). We expressed soma-targeted

306   ChroME in excitatory neurons of the cortex (see Materials and Methods) and performed

307   whole-cell voltage clamp recordings from inhibitory interneurons that do not express

308   ChroME under these conditions, to avoid the confounding effect of direct photocurrents

309   in the patched neuron (Figure 4A). The wide-field fluorescent image (Figure 4B) shows

310   the excitatory neurons (in red) and the patched inhibitory interneuron (in green). We first

311   mapped an 800x800µm^2 FOV at low spatial sampling (40µm grid) to identify the sub-

312   regions that contained most of the presynaptic neurons (Figure 4C). We then re-mapped

313   these sub-regions at fine resolution (20µm/pixel, Figure 4D) and again at even higher

314   resolution (9µm/pixel, Figure 4E). Due to variable opsin protein expression levels across

315   neurons, as well as variable intrinsic neural excitability, neurons are differentially sensitive

316   to light. By mapping the same sub-region at different power levels, we were able to take

317   advantage of this variability of photosensitivities to help identify putative individual (i.e.,

318   'unitary') sources of presynaptic input (Figure 4D). We generated excitatory postsynaptic

319   currents (EPSCs) by sequential photostimulation of the entire volume and observed that

320   most connectivity maps exhibited spatial clusters (Figure 4D-E) as typically observed

321   when mapping synaptic input in space[14]. Within each cluster, most of the postsynaptic

322   responses had similar amplitudes and time courses, suggesting they primarily arose from

323   just one or a small number of presynaptic neurons (Figure 4F-G). We also performed

324   synaptic connectivity mapping *in vivo* (Figure 4—figure supplement 1). These results

325   demonstrate that 3D-MAP is easily scalable and suitable for obtaining high-resolution and

326   large-scale connectivity maps of neural circuits in 3D.

15

A *3D mapping by a single focus*

- ○ Cell w/o opsin
- ▲ Cell with opsin
- ● Stimulation focus
- ◀ Patch-clamp setup

B *Wide-field image*

100μm

C *Coarse mapping*
(40μm/pixel, FOV: 800x800μm²)

ROI in D

nA
1.2

100μm

0

D *Fine mapping* (20μm/pixel, FOV: 652x780μm²)

Representative traces from a single pixel at different powers

ΔZ: -98μm   -65μm   -33μm   0μm

P:
57%
66%
74%
91%
100%

ROI in E

pA
100

0

100μm

10pA
5ms

E *Super fine mapping* (9μm/pixel, FOV: 406x406μm²)

ΔZ=-80μm   ΔZ=-40μm   ΔZ=0μm   ΔZ=40μm   ΔZ=80μm

pA
42

④
⑤
②
①
③

100μm

0

F *Traces from ROI 1-5 in E*

①   ②   ③   ④   ⑤

80pA
25ms

G *Representative traces in ROI 1-5 across different trials*

10pA
5ms

327

16

Figure 4. 3D Mapping of excitatory synaptic connections with 3D-MAP. (A) Schematic diagram of the experiment. A single focus randomly scans the volume adjacent to the patched interneuron that does not express opsin, and the readout map reveals the synaptic connections between photo-activated pyramidal neurons and the patched interneuron. (B) An example of widefield image of opsin-expressing pyramidal neurons (red) and the patched interneuron (green). (C) A coarse 2D map in an 800x800µm^2 FOV at 40µm resolution identifies the sub-regions of the brain slice with presynaptic neurons. (D) Mapping the selected region at higher resolution (green box in C). Each row uses the same stimulation laser power (100% power: 145µW) across multiple axial planes, and each column is a map of the same axial plane at different powers. Representative excitatory postsynaptic currents (EPSCs) traces (right) show how synaptic currents at the same photostimulation pixel change as the stimulation power increases, presumably due to recruitment of additional presynaptic neurons. Data are averaged over 5 repetitions. (E) Super-fine resolution mapping of the region of interest (ROI) (green box in D) in 3D at P=90µW. The green circle in c-e labels the location of the patched interneuron. (F) Traces from ROIs 1-5 labeled in E, averaged over 5 repetitions. (G) Representative traces of single trials without averaging from corresponding ROIs in the same color, measured across three different repetitions. The blue bar on top of traces in F-G indicates the 4ms stimulation time.

One of the major advantages of 3D-MAP over conventional single point scanning approaches[28-30] is that it has the capacity to simultaneously stimulate multiple neurons distributed anywhere in the addressable volume. Multi-site photostimulation is crucial for perturbing or mapping brain circuits because only the activation of neural populations in parallel can drive the sophisticated activity patterns needed to understand network dynamics or behavior[36]. Thus, we next demonstrated that 3D-MAP is able to simultaneously stimulate multiple user-defined targets (Figure 4—figure supplement 2) that we selected according to the connection map in Fig. 4e. While patching the same inhibitory interneuron as described above (Figure 4), we first stimulated the 5 presynaptic ROIs (Figure 4E-F) one-by-one, and then stimulated subsets of them simultaneously, and finally stimulated all the ROIs together (Figure 4—figure supplement 2C). We compared the photocurrents measured by multi-site simultaneous stimulation to the linear sum of individual responses by single stimulation (Figure 4—figure supplement 2D) and observed the multi-site stimulation generates greater net input (Figure 4—figure supplement 2E, p=0.0488 for 2-5 sites stimulation, two-way analysis of variance

17

360   (ANOVA)). This example shows that 3D-MAP is able to simultaneously and flexibly

361   stimulate multiple targets and also can rapidly adjust the 3D patterns in milliseconds,

362   which is critical for online interrogation of neural circuits. Although 3D-MAP could readily

363   co-stimulate many more targets at a time (see below), here we were limited by the number

364   of presynaptically identified neurons.

365

366   ***Reconstructing synaptic networks by multi-site stimulation via gradient descent***

367

368   Physiological brain mapping approaches must overcome the challenge of temporal

369   throughput to map ever larger regions of brain tissue. We reasoned that mapping neural

370   circuits with multiple foci, rather than a single focus, could scale up the temporal

371   throughput of the system dramatically, since the overall connectivity matrix is remarkably

372   sparse. Instead of randomly shifting a single focus to measure the one-to-one synaptic

373   connections (Figure 4), we used 3D-MAP to stimulate multiple random voxels

374   simultaneously and reconstructed the spatial map of presynaptic networks via gradient

375   descent. In our experiment, the positions of the simultaneously stimulated voxels were

376   randomly distributed in the 3D volume and the neural connections are unknown to begin

377   with, unlike co-stimulating known presynaptic ROIs in Figure 4—figure supplement 2. In

378   acute brain slices we again patched a GABAergic interneuron under voltage-clamp mode

379   and recorded both EPSCs, and subsequently, inhibitory postsynaptic currents (IPSCs).

380   We projected random sets of foci (five at a time) and repeated this process until all voxels

381   in 3D were stimulated several times (typically 5-10). Treating the recorded photocurrents

382   as a combination of responses from multiple sites, we then reconstructed the map of the

383   synaptic network using an optimization algorithm based on gradient descent (Figure 5A-

384   B, see Materials and Methods).

18

385

386   Results in Figure 5C-E show the excitatory synaptic network map and inhibitory synaptic

387   network map of the same GABAergic interneuron in an 800x800x200µm^3 volume at three

388   different stimulation powers. Multi-site simultaneous stimulation has two key advantages.

389   First, multi-site stimulation engages the activity of spatially distributed ensembles of

390   neurons (rather than single neurons or small local clusters), which may facilitate

391   polysynaptic network activity and engages network level properties of the circuit. Second,

392   since our approach is compatible with compressed sensing, it becomes possible to

393   reconstruct the same mapping results with fewer measurements compared to single-

394   target stimulation, assuming that the multiple stimulation sites are sparse, and that the

395   readout signal is a linear combination of the inputs from these sites. The assumption is

396   valid when the multiple voxels for concurrent stimulation are randomly drawn from the

397   volume and the number of these voxels is much smaller than the total voxels in the volume

398   (5 voxels are randomly drawn from 1600 voxels in our experiment). Since multiple voxels

399   are stimulated at the same time (say N voxels), each voxel needs to be measured N times

400   with different patterns to estimate the contribution of each voxel to the photocurrent if

401   without compressive sensing. Under the assumption of sparsity and linearity, we can

402   reconstruct the map of neural networks using compressive sensing and with less

403   repetitions (Figure 5—figure supplement 1). This feature of 3D-MAP is critical to speed

404   up the mapping of networks in large volumes where single-target stimulation of every

405   voxel would be prohibitively time-consuming.

19
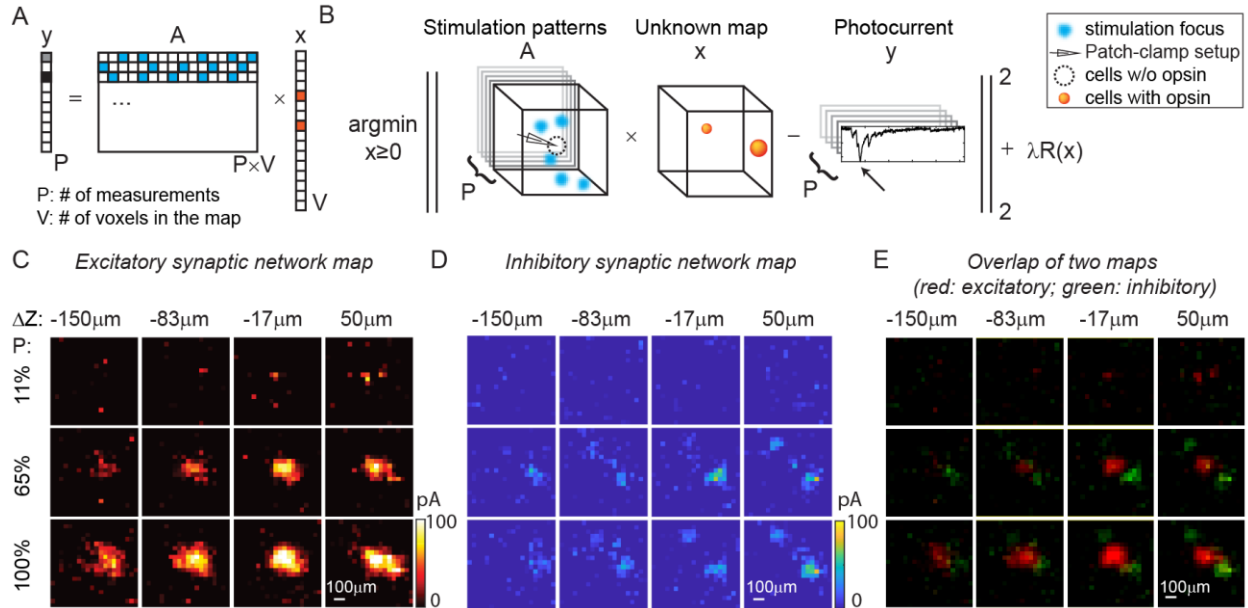
Figure 5. Mapping of synaptic networks *in vitro* by multi-site random simultaneous stimulation and computational reconstruction. (A) The forward model for multi-site random simultaneous stimulation. V, the number of voxels in the 3D volume. P, the number of patterns, which are orthogonal to each other. y, peak value of the measured synaptic currents. A is a matrix, where each row represents an illumination pattern, including 5 foci here (blue, N=5). x is a vector of the unknown synaptic networks to be reconstructed. (B) Inverse problem formulation. The optimal map, x, minimizes the difference between the peak of measured currents (y) and those expected via the forward model, with a regularizer $\lambda R(x)$. (C) Excitatory synaptic connection map of a GABAergic interneuron located at [0, 0, 0]. (D) Inhibitory synaptic connection map from the same cell. (E) Overlap of the excitatory map (red) and inhibitory map (green) to show their spatial relationship. Figures in (C-E) are recorded in an 800x800x200µm³ volume with three different stimulation powers (100% stimulation power is 890µW in total out of the objective lens). The number of simultaneous stimulation foci (N) is five in both cases and the results are average over five repetitions.

All-optical parallel interrogation of a large number of neurons in vivo

All-optical interrogation of neural circuits permits the functional dissection of neuronal

dynamics *in vivo* and can causally relate specific patterns of neural activity to behavior.

So far, this has only been possible in the living mammalian brain with two-photon

holographic optogenetics[13-16,20-22]. Here, we tested whether we can use 3D-MAP for all-

optical interrogation of a large number of neurons *in vivo*, and use visible light but maintain

high spatial precision. To achieve this, we added an optical detection path to 3D-MAP for

20

430 fluorescence imaging (Figure 6A). First, we recorded a widefield image stack by

431 mechanically scanning the objective to identify the location of labeled neurons in 3D. Then,

432 we *simultaneously* photo-stimulated all the identified neurons in the volume with 3D-MAP

433 (a pulse train of 10 pulses at 20Hz, and each pulse is 4ms consisting of 10 projection

434 angles and masks), and recorded calcium activity at 10Hz of all these neurons by

435 widefield imaging with ROI projection using the same DMD (Figure 6A insert plots). Since

436 one-photon widefield imaging has no z-sectioning ability, we took advantage of this

437 feature to capture fluorescence signals from neurons that are above and below the focal

438 plane (dash plane in Figure 6A). To improve the image contrast as well as reduce photo-

439 bleaching, we used 2D patterns computed from the maximum z projection of the widefield

440 image stack to selectively illuminate only the neurons[10] rather than the whole field when

441 recording calcium activity. We started imaging after stimulation of the opsin to avoid

442 artifacts caused by the stimulation light exciting the calcium indicator (inset plot in Figure

443 6A). The start time (t=0) in all the z-scored images refers to the start time of imaging, not

444 the start time of stimulation. We co-expressed the blue-light sensitive opsin soma-

445 targeted stCoChR-p2A-H2B-GFP and the red calcium sensor jRCaMP1a sparsely[37] in

446 L2/3 neurons in the mouse brain[23] via *in utero electroporation* (Figure 6C). We then

447 implemented all-optical 3D-MAP to simultaneously stimulate and image, and selectively

448 interrogate tens of neurons in the mouse brain.

449

450 We first performed a control experiment with acute brain slices to show that the observed

451 changes in fluorescence intensity are indeed due to calcium activity (Figure 6B). We

452 photo-stimulated and imaged 28 neurons simultaneously *in vitro* (see Figure 6—figure

21

453   supplement 1A for the widefield image of the neurons) and we recorded calcium activity

454   from these neurons before and after applying tetrodotoxin (TTX) to block action potentials.

455   Importantly, TTX completely blocked the light-induced calcium transients demonstrating

456   that they are due to calcium influx following light-evoked spiking. The results show

457   obvious changes of fluorescence intensity before applying TTX and no changes after

458   applying TTX (Figure 6B). Therefore, the changes of fluorescence intensity are caused

459   by calcium activity rather than system artifacts.

460

461   All subsequent experiments were then performed *in vivo* in L2/3 neurons that are 200µm-

462   300µm deep (Figure 6—figure supplement 1B) in the intact mouse brain. We first

463   performed a power test to determine the optimal photostimulation power needed to elicit

464   detectable calcium activity in each neuron (Figure 6D). Then, we measured an *in vivo* all-

465   optical 3D PPSF (a measure of calcium fluorescence change as a function of radial and

466   axial displacements of the excitation target) with L2/3 neurons at the optimized power.

467   The all-optical PPSF reflects the spatial specificity of all-optical 3D-MAP, incorporating

468   the optical PSF, opsin sensitivity, and calcium indicator sensitivity, which is yet another

469   system characterization that differs both from the optical PSF and from electrophysiology

470   PPSF. Averaged measurements of all-optical PPSF across 10 neurons indicate a lateral

471   resolution of 49±21µm and an axial resolution of 53±28µm (Figure 6E). An example of

472   calcium traces from 11 positions along the x-axis in the all-optical PPSF measurement is

473   shown in Figure 6—figure supplement 1C. The result demonstrates all-optical 3D-MAP

474   achieves high spatial resolution *in vivo* under the conditions used.

475

476   Next, we tested whether 3D-MAP could photo-activate a large number of neurons *in vivo*

477   in 3D while maintaining spatial specificity. We photo-stimulated and imaged 80 user-

478   selected L2/3 neurons *in vivo* simultaneously with a total power of 480µW out of the

479   objective lens (Figure 6F-G). Figure 6F shows the maximum z projection of a

480   600x600x40µm^3 volume, and Figure 6G shows the calcium activity recorded

481   simultaneously from every jRCaMP1-expressing neuron in the volume. The stimulation

482   pattern is shown in Figure 6—figure supplement 1D and the average separation between

483   neurons is about 49±26µm (Figure 6—figure supplement 1E). The number of neurons

484   stimulated was limited here by the size of FOV and the density of expressing neurons,

485   and potentially could be over one hundred neurons with a larger FOV (see Discussion).

486   These results demonstrate that all-optical 3D-MAP achieves high-throughput
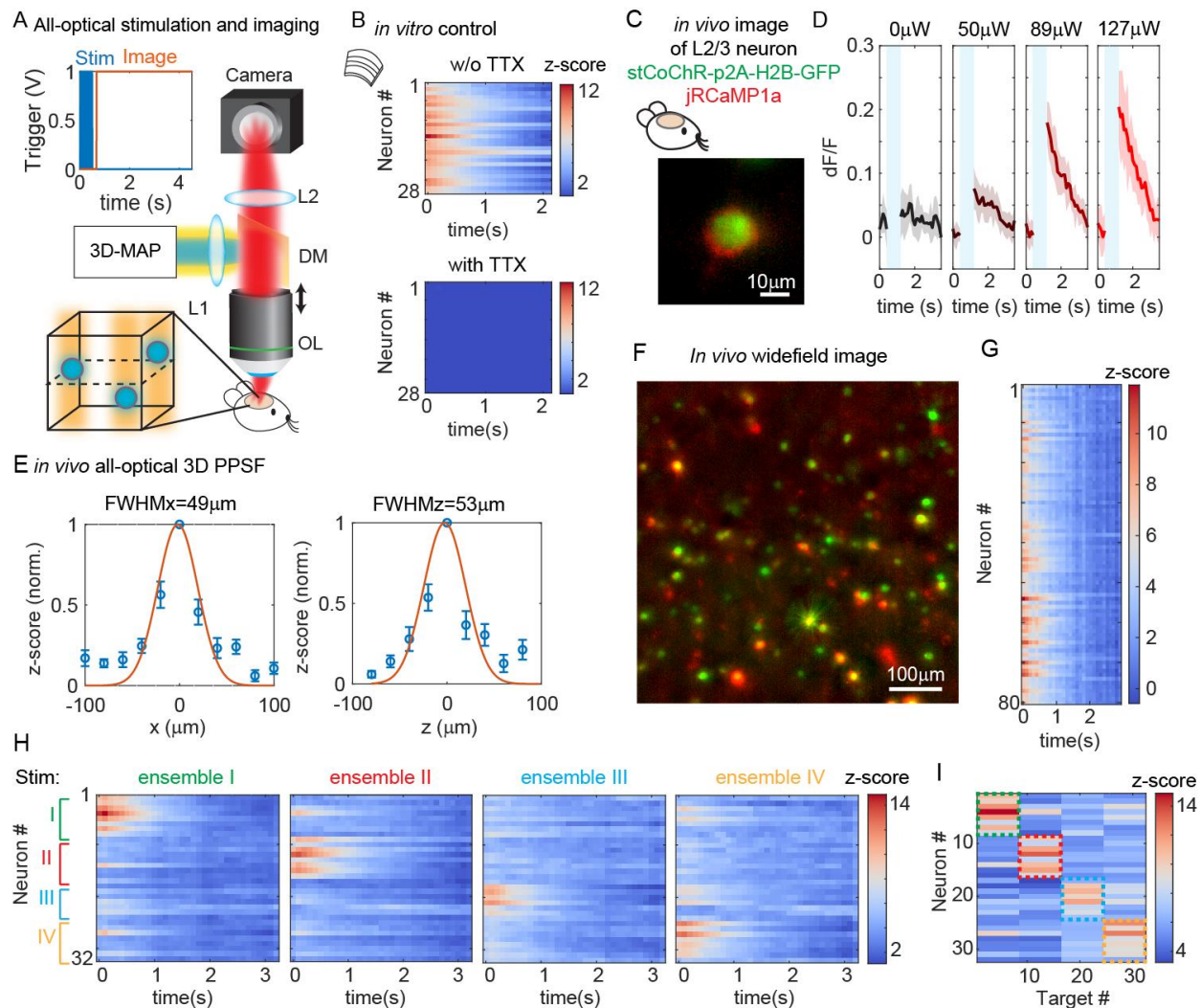
487   photostimulation and imaging of neurons.

488

489   Finally, we tested whether all-optical 3D-MAP can stimulate and image ensembles of

490   spatially intermixed neurons as has been shown with two-photon holographic

491   optogenetics[13,21,24]. The relatively sparse expression of the opsin and calcium sensor

492   here facilitated targeting specificity (mean distance between neurons in the FOV was

493   67±37µm which was larger than the all-optical PPSF, Figure 6—figure supplement 1F).

494   Instead of photo-stimulating all neurons in the volume simultaneously, we randomly

495   assigned 32 neurons to 4 ensembles (8 neurons per ensemble) by Poisson disc sampling

496   and we photo-stimulated each of the four ensembles sequentially while simultaneously

497   imaging all neurons in the four ensembles with patterned illumination (Figure 6H-I). The

498   widefield image of the neurons and the 4 stimulation patterns are shown in Figure 6—

23

499   figure supplement 1G-H. Figure 6H shows the calcium activity of all neurons under

500   different photostimulation patterns, and Figure 6I shows the peak z-score of each neuron

501   versus the stimulated neuron. We observe that neurons exhibit strong calcium activity

502   primarily when they are stimulated, and minimal calcium activity when the adjacent

503   neurons are stimulated. Another example with 30 neurons in 6 ensembles is shown in

504   Figure 6—figure supplement 2. These results demonstrate minimal cross-talk between

505   photo-stimulated ensembles and limited off-target stimulation within the imaging volume

506   even when stimulating and imaging L2/3 neurons *in vivo*. Thus, under relatively sparse

507   opsin-expression conditions, 3D-MAP can be used to photo-activate user-defined

508   spatially intermixed ensembles in the superficial layers of the mouse brain. For densely

509   labeled populations, 3D-MAP could still be used to photo-activate small spatial clusters

510   of neurons which, depending on the goals of the experiments, could still be very

511   informative[8,10].

24

512

513

Figure 6. All-optical simultaneous photostimulation and imaging of groups of neurons at L2/3 in the mouse brain. (A) Experimental setup. The 3D-MAP setup as in Figure 1A is combined with an imaging path using a dichroic mirror, relay lenses, and a camera. Zoom-in view: neurons (blue circles) are stimulated in 3D with 3D-MAP, and calcium activity is recorded from widefield imaging with selective fluorescence excitation (yellow light) by the DMD. The dashed plane indicates the imaging focal plane. Top left: A timing plot shows that fluorescence imaging begins at t=0, immediately after photostimulation. (B) Control experiment with brain slices. Top: calcium activity recorded from 28 neurons. Bottom: same neurons after applying TTX, when no calcium activity is detected. (C) Fluorescent *in vivo* image of a L2/3 neuron that co-expresses stCoChR-p2A-H2B-GFP (green) and jRCaMP1a (red). (D) Power test of a representative neuron, averaged across 10 repetitions. The blue box indicates the period when stimulation laser is on, and the imaging acquisition is off. (E) *in vivo* all-optical 3D PPSF. The lateral resolution is about 49±21μm and the axial resolution is about 53±28μm (n=10 L2/3 neurons). (F) Maximum z projection of an *in vivo* widefield image stack (600x600x40μm^3) of L2/3 neurons, (green, stCoChR-p2A-H2B-GFP; red, jRCaMP1a). (G) Calcium activity of 80 neurons as in f recorded during simultaneous photostimulation and imaging. (H) Calcium activity of 32 neurons that are addressed with four distinct photostimulation patterns (labeled with different colors, also see Figure 6—figure supplement 1H) while fluorescence imaging data is acquired. (I) Peak z-score of each

25

531 calcium trace recorded in H versus the corresponding stimulation patterns. The dashed colored
532 rectangles highlight the neurons that are stimulated in each of the four patterns.
533
534 **Discussion**
535
536 In this study we demonstrated and validated 3D-MAP, a one-photon technique that

537 enables 3D multi-site random access illumination for high precision optogenetic

538 photostimulation and imaging. 3D-MAP combines novel computational and optical

539 advances to offer powerful and versatile optical brain manipulation capabilities. Unlike

540 prior one-photon approaches that have low spatial resolution (DMD-based 2D

541 projection)[8-12] or small FOV (SLM-based 3D CGH)[4-7], 3D-MAP achieves high spatial

542 precision at high speeds and in large 3D volumes, successfully addressing the superficial

543 layers of neurons in the intact brain. 3D-MAP is the first system to achieve 3D multi-site

544 illumination with previously unattainable DoF by simultaneously sculpting the light field in

545 both intensity and angular domains. Therefore, 3D-MAP is able to generate high

546 resolution 3D patterns over large volumes that CGH cannot synthesize. 3D-MAP is also

547 able to project 3D patterns at much faster speeds than CGH, not only because the current

548 refresh rate of DMDs is an order of magnitude faster than that of SLMs, but also because

549 calculating the light field parameters with ray tracing in 3D-MAP is much faster than

550 calculating phase masks in 3D CGH. Perhaps most importantly for the broader

551 neuroscience community, one can build a 3D-MAP system a small fraction of the cost of

552 two-photon holographic optogenetic systems (see Supplement Table 2). At the expense

553 of lower spatial resolution and depth penetration, 3D-MAP is far simpler to operate and

554 maintain and can readily address just as many neurons with far lower laser power. Since

555 many types of circuit investigation experiments do not require the absolute spatial

556 specificity of two-photon approaches[8,10], many groups that would not otherwise leverage

26

557   patterned illumination approaches could adopt 3D-MAP for their optogenetics research

558   applications.

559

560   3D-MAP is the first demonstration that uses 4D light field patterning for *in vivo* optogenetic

561   photostimulation. Even though two-photon photostimulation techniques have combined

562   SLMs with scanning mirrors previously[21,38,39], 3D-MAP is fundamentally different from

563   these techniques because it modulates the 4D light field (x, y, k_x, k_y), so the degrees-of-

564   freedom (DoF) of the system is the *product* of the DMD's and the scanning mirrors' DoF.

565   In previous work, the SLM and scanning mirrors both modulate 2D phase at the same

566   plane (k_x, k_y), so the DoF of the previous systems[21,38,39] is the *sum* of the SLM's and the

567   scanning mirrors' DoF. Hence, 3D-MAP achieves orders-of-magnitude more DoF without

568   extra hardware. A further advantage of 3D-MAP over previous work is that it synthesizes

569   a custom 3D intensity pattern in 3D (x, y, z) with 4D light field control, which is a well-

570   posed problem, whereas controlling 3D intensity with 2D phase control is an ill-posed

571   problem. Note that previous work[40] on 4D light field display also used a DMD, along with

572   a microlens array (MLA), but is fundamentally different from 3D-MAP. First, the DoF of

573   3D-MAP is orders-of-magnitude higher since scanning mirrors have much more DoF than

574   a fixed MLA. Second, the MLA has a built-in tradeoff between spatial and angular

575   resolution whereas 3D-MAP does not. Therefore, the maximum defocus range of 3D-

576   MAP is 720μm (Figure 2—figure supplement 1A) whereas the MLA-based method only

577   achieves 40μm range in microscopy applications. Third, we demonstrated 3D-MAP with

578   acute brain slices and *in vivo* mouse brain where tissue scattering distorts the light field

579 and limits the resolution, whereas the previous work is not used for optogenetics under

580 scattering.

581

582 As a proof-of-principle experiment, we demonstrated all-optical 3D-MAP in a relatively

583 thin 3D volume (600x600x40µm^3) where two opsin-expressing neurons right on top of

584 each other along the z-axis is very rare under the conditions of relatively sparse labeling[37].

585 Also, because we used a patterned widefield imaging system to detect the fluorescence

586 emitted from calcium indicators, the signal-to-noise ratio of the fluorescence images will

587 be lower than the readout noise of the camera if the neuron is too far away from the focal

588 plane. To enable 3D detection over a larger axial range, one could apply pupil encoding[34],

589 light-field detection[41,42], or remote focusing[43] to the imaging path of 3D-MAP.

590

591 Both one-photon and two-photon multi-site photostimulation are subject to spatial cross-

592 talk, as out-of-focus light from one target may accidentally stimulate neurons that are at

593 other focal planes, especially when the density of foci is high or when out-of-focus

594 neurons are more photosensitive than the desired targets. In Figure 6, we demonstrated

595 that the cross-talk in our experiment is minimal under conditions of relatively sparse opsin

596 expression as obtained with conventional *in utero* electroporation[37]. However, when the

597 separation between two adjacent neurons is closer than the all-optical PPSF, off-target

598 effects are likely, even under sparse expression conditions. Therefore, in addition to

599 expression sparsity, we can also control the stimulation pattern's sparsity to mitigate

600 spatial cross-talk. When the desired density of foci is high and cross-talk is expected, 3D-

601 MAP could potentially leverage its multi-kHz patterning speed to exploit the temporal

28

602   domain by multiplexing patterns and targeting smaller subsets of neurons at a time in

603   order to increase pattern sparsity.

604

605   The maximum number of neurons that can be co-stimulated without cross-talk in one-

606   photon or two-photon photostimulation depends on the available laser power, the limits

607   of brain heating, the spatial resolution of the system, the FOV, and the spacing of opsin-

608   expressing neurons. Compared to two-photon photostimulation, 3D-MAP trades on

609   spatial resolution (by a factor of 2-3 in superficial layers) to use 2-3 orders lower laser

610   power. For example, two-photon photostimulation techniques typically restrict the

611   instantaneous power under the objective below 4W to avoid photodamage[16,24]. At full

612   power, two-photon photostimulation techniques can simultaneously activate tens to over

613   a hundred neurons[16,21,24,44]. In contrast, 3D-MAP is able to photostimulate dozens of

614   neurons simultaneously with only 480µW out of the objective (Figure 6F-G). 3D-MAP

615   requires sparser expression than for two-photon stimulation to achieve comparable

616   effective specificity, but since total needed power is nearly 100-fold less for comparable

617   stimulation patterns, brain heating is much less of a concern, and the technique can be

618   scaled up to address more neurons in a larger brain area. Many experiments do not need

619   full optical control over all neurons in a volume – for example, when targeted a specific

620   transcriptional subtype, and many other experiments do not absolutely require single-cell

621   specificity. Thus, for many applications 3D-MAP should be preferable to two-photon

622   applications, with the specific exceptions of experiments that demand photo-stimulation

623   of precise ensembles within a small volume of densely labeled tissue, or when the neural

624   targets are located at brain depths only accessible to infrared light. The simplicity and

29

625 scalability of 3D-MAP thus provides new experimental capabilities that two-photon

626 photostimulation techniques cannot easily achieve.

627

628 Like any other one-photon photostimulation technique, the effective resolution of 3D-MAP

629 in brain tissue is determined by scattering. As we show in Figure 2 and Figure 6,

630 illumination with red shifted sources can reduce Rayleigh scattering and mitigate

631 resolution loss through brain tissue, but the accessible depth remains fundamentally

632 limited to the first few hundreds of microns below the surface of the mouse brain and the

633 scattering effect is more severe the deeper the stimulation is. To photo-stimulate neurons

634 deeper inside the mammalian brain with 3D-MAP, the cortex can be surgically

635 removed[10,45-46] or implemented with a miniaturized microscope[6,47] as it is routinely

636 performed to image deep structures such as the hippocampus or the thalamus. Taken

637 together, 3D-MAP is a new volumetric optogenetic projection system that offers major

638 advantages over existing one-photon and two-photon optogenetic technologies and

639 should facilitate a wide range of neural perturbation experiments to map the structure and

640 function of brain circuits.

641

642 **Materials and Methods**

643

644 **Ethical statement.** All animal experiments were performed in accordance with the

645 guidelines and regulations of the Animal Care and Use Committee of the University of

646 California, Berkeley.

647

648 **Data availability.** The datasets generated during and/or analyzed during the current

649 study are available upon reasonable request to the corresponding authors.

30

650

651 **Code availability.** Custom code used to collect and analyze data is programed in

652 MATLAB. The code has been deposited in Github (https://github.com/Waller-Lab/3D-

653 MAP).

654

655 **3D-MAP optical setup.** The laser sources for optogenetic stimulation are Diode Pumped

656 Solid State (DPSS) laser diodes. One is at 473nm wavelength (MBL-N-473A-1W,

657 Ultralasers, Inc., Canada) and the other at 635nm wavelength (SDL-635-LM-5000T,

658 Shanghai Dream Lasers Technology Co., Ltd., China) for different opsins. The results

659 shown in Figure 5 and Figure 3—figure supplement 1E-H are measured under red

660 stimulation, and all the others are stimulated by blue light. The laser source for *in vivo*

661 PPSF (Figure 3H-J), the wide-field imaging (Figure 4B), and calcium imaging (Figure 6,

662 Figure 6—figure supplement 1-2) is a DPSS laser at 589nm wavelength (MGL-W-589-

663 1W, Ultralasers, Inc., Canada). Current supplies are externally driven by an analog

664 modulation voltage. The laser beams are scanned by a pair of galvo-mirrors (GVS202,

665 Thorlabs, Inc., U.S.), and then the beam size is expanded to fill the DMD (DLP9000X and

666 the controller V4390, ViALUX, Germany) by a 4-f system (f_1=45mm, f_2=150mm). The

667 DMD is mounted on a rotation base in order to maximize the output laser power from 'ON'

668 pixels and minimize the diffraction pattern from DMD pitches. Then the patterned beam

669 passes through a tube lens (f=180mm) and the objective lens (XLUMPlanFL N, 20x, NA

670 1.0, Olympus) to generate multiple foci. The objective lens is mounted on a motorized z-

671 stage (FG-BOBZ-M, Sutter Instrument, U.S.). A custom dichroic mirror

672 (zt473/589/635rpc-UF2, Chroma, U.S.) is placed before the objective lens to reflect the

673 stimulation laser beams while transmitting fluorescence photons emitted from the sample.

674   The fluorescence passes through a tube lens (f=180mm) and a 4-f system (f$_1$=100mm,

675   f$_2$=150mm), and then is imaged by a camera (Prime95B, Teledyne Photometrix, U.S.,

676   Figure 4B, Figure 6). Brain samples (acute brain slices and anesthetized mice) are placed

677   on a motorized x-y stage (X040528 and the controller MP-285, Sutter Instrument, U.S.).

678   The 3D PSF and patterns (Figure 2 and Figure 2—figure supplement 1) are measured by

679   capturing the fluorescence excitation in a thin fluorescent film on a microscope slide, with

680   a sub-stage objective (XLUMPlanFL N, 20x, NA 1.0, Olympus) coupled to a camera

681   (DCC1545M, Thorlabs, U.S.). Tomographic renderings of the 3D-MAP illumination

682   patterns are obtained by mechanically scanning the illumination objective along the

683   optical (z) axis and recording the 2D fluorescence image stacks at linearly spaced depths

684   with the sub-stage camera. For Figure 3A-D and Figure 4D-E, the targeted positions in

685   the 3D pattern are stimulated in a random order: two sequential stimulations are

686   separated by a minimum distance calculated by Poisson disc sampling in order to avoid

687   photocurrent accumulation caused by repeat stimulations. A NI-DAQ (National

688   Instruments, NI PCIe-6363) synthesizes custom analog signals to synchronously

689   modulate the lasers, the galvo-mirrors, the digital triggers to flip frames on the DMD, the

690   trigger signals to the camera as well as the z-stage. An analog input channel enabling

691   synchronous measurements of neural photocurrents and spikes in direct response to the

692   custom 3D light sculpting sequence. A custom MATLAB (MathWorks, U.S.) graphic user

693   interface is used to control the NI DAQ boards, calibrate and align the photostimulation

694   and imaging modalities, and for data acquisition and processing.

695

696 **Synchronized control of 3D-MAP.** The key mechanism to generate a focus on the

697 shifted focal plane by 3D-MAP is to synchronize the scanning mirrors that control the

698 angle of light (ϕ_{SM}, θ) (Figure 7A) and the DMD that controls the amplitude apertures.

699 Figure 7A shows an example of synthesizing a focus below the native focal plane with 10

700 beams in 4ms. The color of circular apertures and lines indicates the time stamp of the

701 DMD apertures and corresponding projection angles. To better show the 3D view in

702 Figure 7A, we plot the positions of DMD apertures and the projection angles in a 2D view

703 (Figure 7B-C). The first aperture is located at $\phi_{DMD} = 0$ (dark blue circle, Figure 7A-B),

704 and the corresponding projection angle is $\phi_{SM} = \pi$ (dark blue lines, Figure 7A, C). To

705 project the angle $\phi_{SM} = \pi$, we apply -2V voltage to the x-axis scanning mirror and 0V to

706 the y-axis scanning mirror (Figure 7C-D). Similarly, we can easily compute the other

707 projection angles and the aperture positions by evenly dividing 2π by the number of

708 beams. The voltage outputs to control the laser intensity, trigger DMD projection, and

709 projection angles of the scanning mirrors are shown in Figure 7D. DMD projects the 10

710 apertures sequentially (Figure 7E) controlled by the TTL trigger signal (purple line, Figure

711 7D), while the scanning mirrors project the corresponding angles controlled by the

712 sinusoidal signal (red line, voltage of x-axis scanning mirror; yellow line, voltage of the y-

713 axis scanning mirror). Strictly, the scanning mirrors voltage should not change during the

714 projection of one beam. However, because the time is very short (0.3ms in Figure 7D),

715 the change of projection angle during this time is negligible. Therefore, synchronizing the

716 DMD and the scanning mirrors is straightforward and only involves calculating the voltage

717 outputs and the DMD patterns as shown in Figure 7D-E.

33
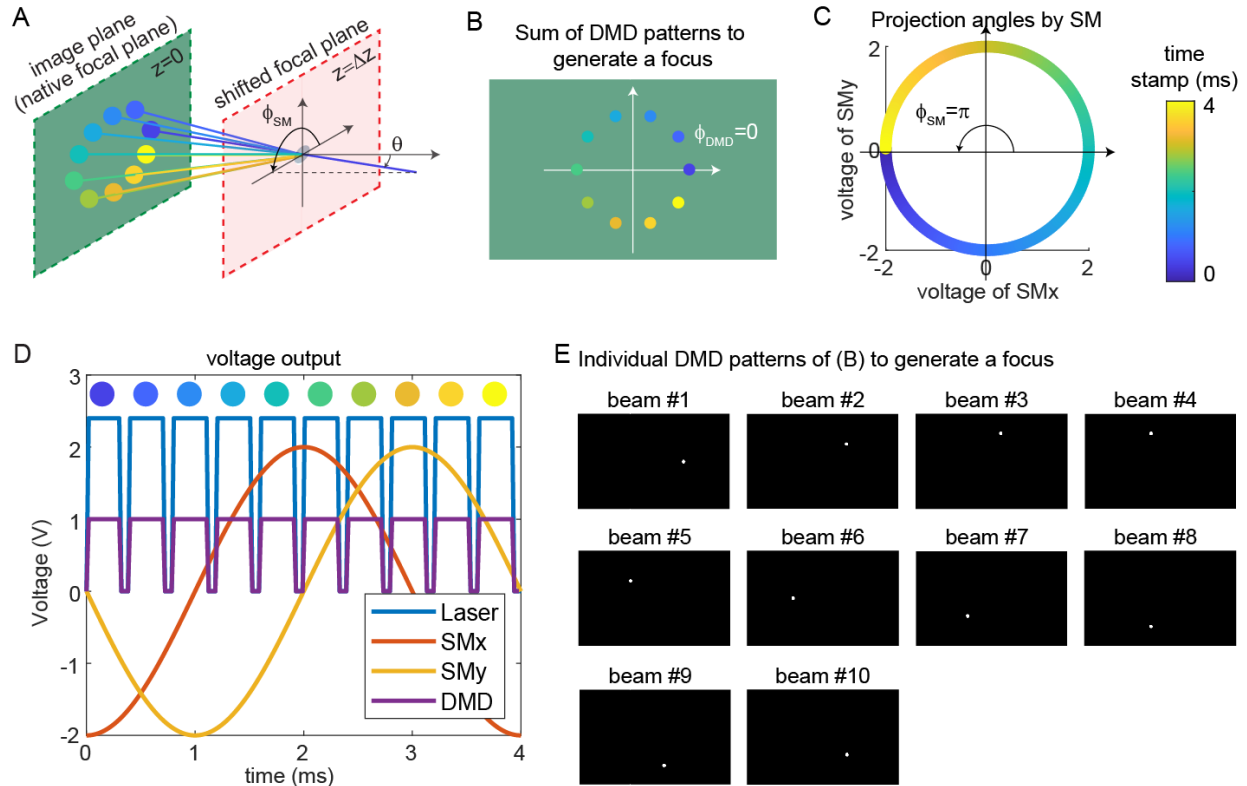
Figure 7. Synchronized control of the scanning mirrors and the DMD to generate a focus at a shifted focal plane by 3D-MAP. (A) A focus spot is generated by 10 beams in 4ms in total. The DMD is located at the relayed image plane projecting 10 apertures sequentially. Scanning mirrors control the corresponding projection angles (ϕ_{SM}, θ) for each beam. θ is the same for all beams and ϕ_{SM} varies. The color of the apertures and the projection angles shows their respective time stamp. (B) 2D view of the image plane in A, showing all 10 apertures on the DMD that are used to generate the focus. The first aperture (dark blue circle) is at $\phi_{DMD} = 0$ and the 10 apertures are evenly distributed in the range of $\phi_{DMD} = (0, 2\pi)$. (C) Projection angles by scanning mirrors. The first projection angle to generate the focus in a with the first aperture in B is located at $\phi_{SM} = \pi$. The scanning mirrors evenly scan along a circular trace in the 4ms stimulation time. (D) The voltage outputs control the hardware. The scanning trace in C is generated by applying sinusoidal signals (red, yellow) to the scanning mirrors. The maximum voltage of the sinusoidal signal decides θ and the phase of the sinusoidal signal decides ϕ_{SM}. The DMD projection is controlled by the TTL signal (purple), which has 10 rising edges in the 4ms stimulation time to project 10 patterns sequentially. The laser intensity is controlled by an analog signal (blue) that is synchronized with the DMD. (E) The 10 patterns to be projected by the DMD to synthesize the focused spot.

Simulation results for typical misaligned examples and correct examples are shown in Figure 8. When the phase of DMD and the phase of the scanning mirrors are misaligned (Figure 8A), 3D-MAP cannot generate a tight focus at the shifted focal plane. Instead, the

34

739   shape at the shifted focal plane looks like a ring (a paraboloid in 3D). To correct the phase

740   mismatch, we can simply adjust ϕ_{DMD} or ϕ_{SM} to change the relative phase between the

741   DMD patterns and the projection angles and correct for any system misalignment. For

742   example, we can change ϕ_{SM} from $\frac{4\pi}{5}$ to π, as a result, the shape at the shifted focal plane

743   will change from a ring to a spot (Figure 8C). Another misalignment may happen when

744   the scanning mirrors have asymmetric response (Figure 8B), which generates an elliptical

745   scanning trace rather than a circular trace. This type of misalignment degrades the focus

746   of 3D-MAP exactly like optical astigmatism. To correct the asymmetric response of the

747   scanning mirrors, we can adjust the amplitude of the voltage output to the scanning

748   mirrors until we obtain a tight focus as in Figure 8C. In addition, adding a π-phase shift to

749   the DMD patterns or the projection angles can generate a focus below (Figure 8C) or

750   above (Figure 8D) the native focal plane.

35

751
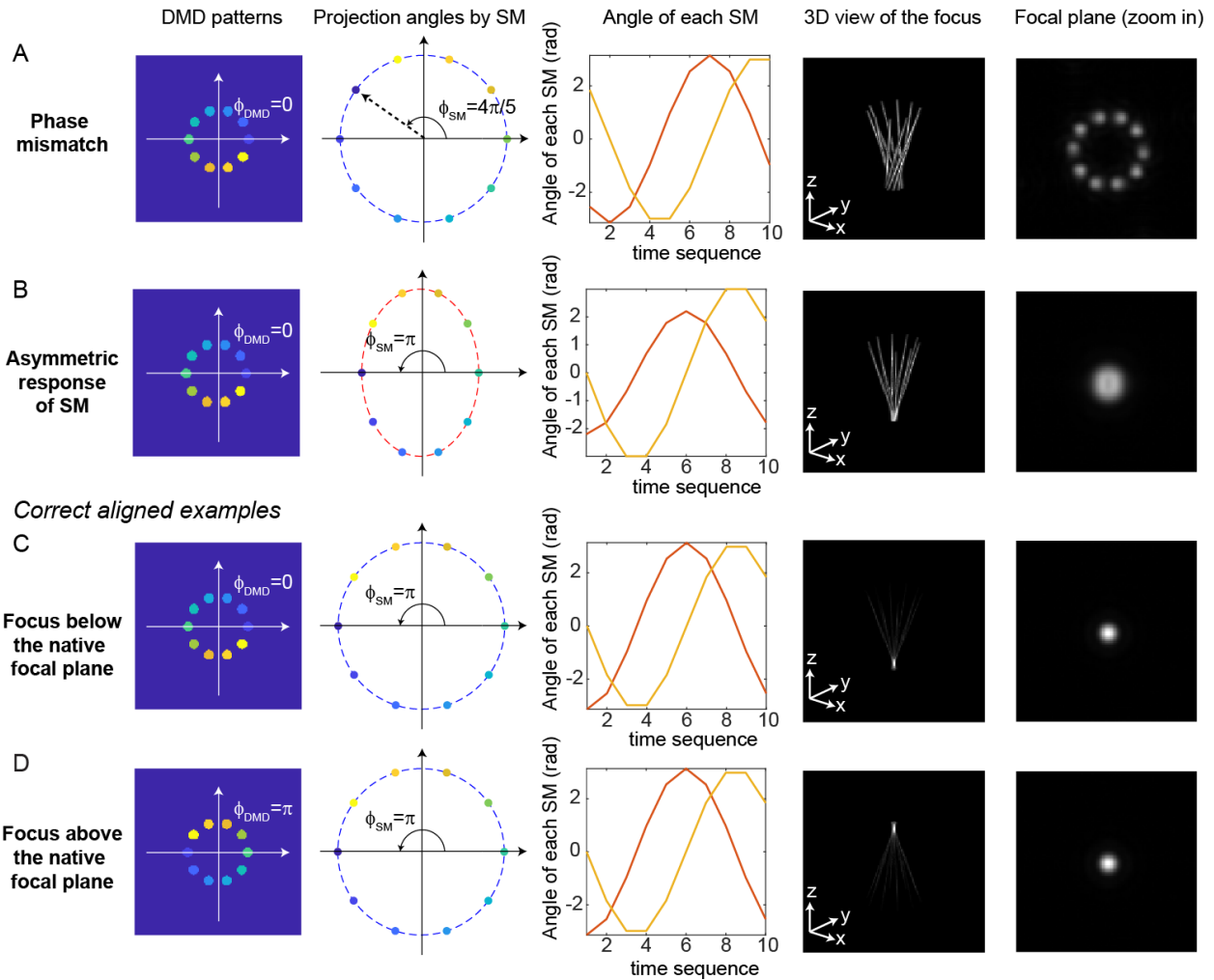
Figure 8. Misaligned examples (A, B) and correct aligned examples (C, D) with 3D-MAP. The first column shows the sum of 10 DMD patterns to generate the focus. The second column shows the projection angles by the scanning mirrors (SM). The color labels the timestamp of the projection as in Figure 7. The third column shows the angle of the scanning mirror in the x-axis (red) and the angle of the scanning mirror in the y-axis (yellow) for the sequential 10 projections, respectively. The fourth column shows the 3D view of the focus (distorted or tightly focused). The fifth column shows the 2D XY-view at the in-focus plane. To show the focus better, the images are zoomed in compared to the images in the fourth column. (Aa) Misaligned example of phase mismatching. The 10 beams cannot overlap to generate a tight focus, instead, a ring is generated at the shifted focal plane. (B) Misaligned example of asymmetric response of the scanning mirrors. The beams in the tangential direction and in the sagittal direction overlap at different locations along the z-axis like astigmatism, generating a distorted focus. (C) Correct aligned example generates a focus below the native focal plane (same as Figure 7). (D) Correct aligned example generates a focus above the native focal plane by adding a π-phase shift to the DMD patterns.

766

36

767   **Computational reconstruction framework.** 3D-MAP projects N foci simultaneously in

768   a 3D volume (V voxels), which is defined as a stimulation pattern (i^{th} pattern A_i). The

769   positions of the N foci are randomly selected from the V voxels. The electrophysiology

770   readout (excitatory postsynaptic currents, EPSCs; or inhibitory postsynaptic currents,

771   IPSCs) under this pattern is recorded and the maximum absolute value of the EPSCs or

772   IPSCs is the measurement y_i under the illumination of ith pattern. Thus, the forward

773   model of multi-site random simultaneous illumination is (Figure 5A):

774   $$y_i = \sum_{j=1}^{V} A_{i,j} x_j, \ i = 1, 2, \ldots, P.$$

775   P is the number of patterns, and all patterns are orthogonal to each other. To solve the

776   synaptic connection map at the jth voxel (x_j), the number P should be equal to V. The

777   reconstruction framework can be formulated as a l_1- regularized optimization problem

778   that seeks to estimate x by minimizing the difference between the measured currents (y)

779   and those expected via the forward model (Figure 5B):

780   $$\underset{x \geq 0}{\arg\min}(\|Ax - y\|_2^2 - \lambda R(x)),$$

781   where $R(x)$ describes total-variation (TV) regularization defined as

782   $$R(x) = \sum_{j=1}^{V} |x_{j+1} - x_j|.$$

783   This optimization problem is solved using fast iterative shrinkage-thresholding algorithm

784   (FISTA), which is a first-order gradient descent algorithm. FISTA is able to reconstruct

785   the result (Figure 5C-D, Figure 5—figure supplement 1) in real time during the

786   experiments. The algorithm is summarized in Algorithm 1.

787

788   Algorithm 1. 3D-MAP algorithm

789

790   1. **Procedure** 3D-MAP multi-sites mapping reconstruction
791   2. Initialize x_0 by uniformly distributed random numbers between [0 1]

37

792   3. $k \leftarrow 0$
793   4. **while** $k < maxiter$ **do**
794   a. Gradient $\Delta x \leftarrow FISTA[x_0, A, y, \lambda]$
795   b. $x_{k+1} = x_k - \mu \Delta x_k$, where μ is the step size
796   c. $k = k + 1$
797   5. **return** x

798
799

800   If every voxel is illuminated M times (the number of repetitions) using P patterns and each

801   pattern illuminates N voxels, we can draw the relation between these parameters:

802     $$P = MV/N.$$

803   To solve x, P should be equal to V, that is, the number of repetitions (M) should equal to

804   the number of foci (N) in each pattern. However, the number of repetitions could be

805   smaller than M if the multiple illumination foci satisfy these two assumptions: first, the foci

806   are distributed sparsely in the volume; second, the readout postsynaptic current is a linear

807   combination of the response from presynaptic neurons stimulated by these foci. As shown

808   in Fig. S6, where the number of foci is five (N=5), it is possible to reconstruct the synaptic

809   connection map coarsely with less than five repetitions (M=1-4) with compressive sensing

810   algorithms.

811
812   **Animal preparation and electrophysiology**

813   Neonatal mice age P3-P4 (wild type, emx1-IRES-Cre (JAX stock#005628), or emx1-

814   Cre;GAD67-GFP (MGI:3590301)) were cryoanesthetized on ice and mounted in a head

815   mold. AAVs driving Cre-dependent expression of either soma-targeted ChroME (Figure

816   4), Chrimson (Figure 5), ChRmine (Figure 3—figure supplement 1), or soma-targeted

817   CoChR (Figure 6 and Figure 6—figure supplement 1-2) were injected via a Nanoject3

818   (Drummond) into the visual cortex (~1-2 mm lateral to lambda, 3 sites, 22 nL/ site), ~100-

819   300 microns below the brain surface. In wild type mice we injected AAV-mDlx-ChroME to

38

820 drive opsin expression in cortical interneurons. All expression vectors co-expressed

821 nuclear targeted mRuby3 except those in the all-optical interrogation experiments (Figure

822 6 and Figure 6—figure supplement 1-2). Mice were used for brain slice or *in vivo*

823 recordings at P28-P56. Brain slices were prepared as previously described[48]. Slices were

824 transferred to a chamber and perfused with ACSF (no receptor blockers) warmed to ~33

825 degrees Celsius. First the microscope objective was centered over the area of V1 with

826 the highest expression density of the opsin, as indicated by the density of mRuby3-

827 expressing cells. ACSF contained in mM: NaCl 119, KCl 2.5, $MgSO_4$ 1.3, NaH_2PO_4 1.3,

828 glucose 20, $NaHCO_3$ 26, $CaCl_2$ 2.5. Internal solutions contained $CsMeSO_4$ (for voltage

829 clamp) or KGluconate (for current clamp) 135 mM and NaCl 8 mM, HEPES 10 mM,

830 Na_3GTP 0.3 mM, MgATP 4 mM, EGTA 0.3 mM, QX-314-Cl 5 mM (voltage clamp only),

831 TEA-Cl 5mM (voltage clamp only). For loose-patch experiments pipettes were filled with

832 ACSF. The resistance of the patch electrodes ranged from 3-5 megaohms. For direct

833 recording of photocurrents or light induced spiking, we patched neurons (either in loose

834 patch or whole cell patch clamp) that expressed mRuby3. For recording light-driven

835 synaptic inputs we patched from unlabeled putative interneurons (that did not have

836 pyramidal morphology), or from GFP-expressing neurons in GAD67-GFP mice.

837

838 For optogenetic mapping we generated light spots ~10 microns wide (apertures of 10-20

839 pixels in radius on DMD). The total stimulation duration was 3-6 milliseconds. For

840 ChroME-expressing (Figure 3A-E, Figure 4) and CoChR-expressing (Figure 6 and Figure

841 6—figure supplement 1-2) animals we used 473 nm light, and for Chrimson and ChRmine

842 we used 635 nm light (Figure 5, Figure 3—figure supplement 1). All mapping used fully

843   randomized sequences. For measurement of PPSFs and multi-spot synaptic maps we

844   used the system in full 3D mode (Figure 3, Figure 5, Figure 4—figure supplement 1-2).

845   For single spot synaptic maps all photo-stimuli were at the native focal plane, and the

846   microscope was moved mechanically under software control to obtain input maps at

847   different axial planes (Figure 4 and Figure 4—figure supplement 1). Mapping at the native

848   focal plane requires only one DMD mask per light stimulus as compared to ten for a full

849   3D pattern, allowing for many more masks to be stored in the DMD RAM and rapidly

850   displayed. Scanning mirrors scan continuously in 2π to enable z-section when mapping

851   at the native focal plane, which is different from direct 2D projection. At the beginning of

852   each mapping experiment, we first took a ten-point laser-power dose response curve of

853   the photocurrent or light-induced synaptic current and used this data to choose the power

854   range for photocurrent or synaptic mapping. For spiking PPSFs, the lowest light level that

855   reliably generated spikes when directly targeting the soma was used. For single spot

856   mapping we updated the DMD pattern at 40-80 Hz. For multi-spot mapping we updated

857   the DMD pattern at 10-20 Hz, which minimized network adaptation.

858

859   For *in vivo* electrophysiology recording and all-optical interrogation, mice were sedated

860   with chlorprothixene (0.075 mg) and anesthetized with isoflurane (1.5-2%). A small

861   stainless steel plate was attached to the skull with Metabond. The skull was protected

862   with cyanoacrylate glue and dental cement (Orthojet). A 2.5 mm craniotomy was made

863   over V1 with a circular biopsy punch. The dura was removed with fine forceps and the

864   craniotomy   was   covered   with   1.2%   agarose   in   ACSF   and   additional   ACSF

865   (electrophysiology) or covered with a cranial window (all-optical interrogation). The mouse

40

866 was then injected with urethane for prolonged anesthesia (0.04 g), and supplemented

867 with 0.5-1.5% isoflurane at the recording rig. Body temperature was maintained at 35-37

868 degrees Celsius with a warming blanket. Neurons were recorded under visualization

869 either with epifluorescence (to target opsin expressing neurons in the upper 100 microns

870 of the brain for PPSF measurements) or in L2/3 via oblique infrared contrast imaging via

871 an optic fiber (200μm diameter) placed at a ~25 degree angle from horizontal located as

872 close as possible to the brain surface underneath the objective. The same procedure for

873 optogenetic mapping used *in vitro* was used *in vivo*. All data analysis was performed in

874 MATLAB.

875

883

884 **Author contributions**

885 All authors contributed to the development of 3D-MAP. N.P. developed the pilot version

886 of electrophysiology-only 3D-MAP and the algorithm of 3D image synthesis. Y.X.

887 designed and assembled the current experimental setup, performed all the experiments,

888 developed the optimization reconstruction algorithm, and performed data processing in

889 all sections. H.A. designed and performed electrophysiology experiments in mouse brain

890 slice and in anesthetized mouse and advised the research. Y.X. and H.A. wrote the

891 manuscript with additional input form N.P and L.W.. L.W. helped advise Y.X. and N.P.

892

References

894

895 1. Deisseroth, K. Optogenetics. *Nat. Methods* **8**, 26–29 (2011).

896 2. Zhang, F. *et al.* Multimodal fast optical interrogation of neural circuitry. *Nature* **446**, 633–
897   639 (2007).

898 3. Ronzitti, E. et al. Recent advances in patterned photostimulation for optogenetics. J. Opt.
899   19, 113001 (2017)

900 4. Lutz, C. et al. Holographic photolysis of caged neurotransmitters. Nat. Methods 5, 821–
901   827 (2008)

902 5. Anselmi, F., Ventalon, C., Bègue, A., Ogden, D. & Emiliani, V. Three-dimensional imaging
903   and photostimulation by remote-focusing and holographic light patterning. *Proc. Natl.*
904   *Acad. Sci. U. S. A.* **108**, 19504–19509 (2011).

905 6. Szabo, V., Ventalon, C., De Sars, V., Bradley, J. & Emiliani, V. Spatially selective
906   holographic photoactivation and functional fluorescence imaging in freely behaving mice
907   with a fiberscope. *Neuron* **84**, 1157–1169 (2014).

908 7. Reutsky-Gefen, I. et al. Holographic optogenetic stimulation of patterned neuronal activity
909   for vision restoration. Nat. Commun. 4, 1509 (2013)

910 8. Dhawale, A. K., Hagiwara, A., Bhalla, U. S., Murthy, V. N. & Albeanu, D. F. Non-redundant
911   odor coding by sister mitral cells revealed by light addressable glomeruli in the mouse.
912   Nat. Neurosci. 13, 1404–1412 (2010)

913 9. Leifer, A. M., Fang-Yen, C., Gershow, M., Alkema, M. J. & Samuel, A. D. T. Optogenetic
914   manipulation of neural activity in freely moving Caenorhabditis elegans. Nat. Methods 8,
915   147–152 (2011)

916 10. Adam, Y. *et al.* Voltage imaging and optogenetics reveal behaviour-dependent changes
917   in hippocampal dynamics. *Nature* **569**, 413–417 (2019).

918 11. Werley, C. A., Chien, M.-P. & Cohen, A. E. Ultrawidefield microscope for high-speed
919   fluorescence imaging and targeted optogenetic stimulation. *Biomed. Opt. Express* **8**,
920   5794–5813 (2017)

921 12. Sakai, S., Ueno, K., Ishizuka, T. & Yawo, H. Parallel and patterned optogenetic
922   manipulation of neurons in the brain slice using a DMD-based projector. *Neurosci. Res.*
923   **75**, 59–64 (2013).

924 13. Carrillo-Reid, L., Han, S., Yang, W., Akrouh, A. & Yuste, R. Controlling Visually Guided
925   Behavior by Holographic Recalling of Cortical Ensembles. *Cell* **178**, 447–457.e5 (2019).

926 14. Naka, A. *et al.* Complementary networks of cortical somatostatin interneurons enforce
927   layer specific control. *Elife* **8**, (2019).

928 15. Daie, K., Svoboda, K. & Druckmann, S. Targeted photostimulation uncovers circuit motifs
929   supporting short-term memory. *Nat. Neurosci.* **24**, 259–265 (2021)

16. Sridharan, S. *et al.* High performance microbial opsins for spatially and temporally precise perturbations of large neuronal networks. *bioRxiv* 2021.04.01.438134 (2021) doi:10.1101/2021.04.01.438134

17. Nikolenko, V. *et al.* SLM Microscopy: Scanless Two-Photon Imaging and Photostimulation with Spatial Light Modulators. *Front. Neural Circuits* **2**, 5 (2008).

18. Papagiakoumou, E. *et al.* Scanless two-photon excitation of channelrhodopsin-2. *Nat. Methods* **7**, 848–854 (2010).

19. Pégard, N. C. *et al.* Three-dimensional scanless holographic optogenetics with temporal focusing (3D-SHOT). *Nat. Commun.* **8**, 1228 (2017).

20. Gill, J. V. *et al.* Precise Holographic Manipulation of Olfactory Circuits Reveals Coding Features Determining Perceptual Detection. *Neuron* **108**, 382–393.e5 (2020)

21. Marshel, J. H. *et al.* Cortical layer-specific critical dynamics triggering perception. *Science* **365**, (2019)

22. Robinson, N. T. M. *et al.* Targeted Activation of Hippocampal Place Cells Drives Memory-Guided Spatial Behavior. *Cell* **183**, 1586–1599.e10 (2020)

23. Forli, A., Pisoni, M., Printz, Y., Yizhar, O. & Fellin, T. Optogenetic strategies for high-efficiency all-optical interrogation using blue light-sensitive opsins. *Elife* **10**, (2021)

24. Mardinly, A. R. *et al.* Precise multimodal optical control of neural ensemble activity. *Nat. Neurosci.* **21**, 881–893 (2018).

25. Podgorski, K. & Ranganathan, G. Brain heating induced by near-infrared lasers during multiphoton microscopy. J. Neurophysiol. 116, 1012–1023 (2016)

26. Sun, S., Zhang, G., Cheng, Z., Gan, W. & Cui, M. Large-scale femtosecond holography for near simultaneous optogenetic neural modulation. *Opt. Express* **27**, 32228–32234 (2019).

27. Yang, S. J. et al. Extended field-of-view and increased-signal 3D holographic illumination with time-division multiplexing. Opt. Express 23, 32573–32581 (2015)

28. Petreanu, L., Mao, T., Sternson, S. M. & Svoboda, K. The subcellular organization of neocortical excitatory connections. Nature 457, 1142–1145 (2009)

29. Losavio, B. E., Iyer, V., Patel, S. & Saggau, P. Acousto-optic laser scanning for multi-site photo-stimulation of single neurons in vitro. J. Neural Eng. 7, 045002 (2010)

30. Wang, K. et al. Precise spatiotemporal control of optogenetic activation using an acousto-optic device. PLoS One 6, e28468 (2011)

31. Zhang, J., Pégard, N., Zhong, J., Adesnik, H. & Waller, L. 3D computer-generated holography by non-convex optimization. *Optica, OPTICA* **4**, 1306–1313 (2017).

32. GERCHBERG & W, R. A practical algorithm for the determination of phase from image and diffraction plane pictures. Optik 35, 237–246 (1972)

33. Leseberg, D. Computer-generated three-dimensional image holograms. Appl. Opt. 31, 223–229 (1992)

34. Xue, Y. *et al.* Scanless volumetric imaging by selective access multifocal multiphoton microscopy. *Optica* vol. 6 76 (2019).

35. Hossein Eybposh, M., Caira, N. W., Atisa, M., Chakravarthula, P. & Pégard, N. C. DeepCGH: 3D computer-generated holography using deep learning. *Opt. Express* **28**, 26636–26650 (2020)

43

36. Li, N., Daie, K., Svoboda, K. & Druckmann, S. Robust neuronal dynamics in premotor cortex during motor planning. Nature 532, 459–464 (2016)

37. Adesnik, H. & Scanziani, M. Lateral competition for cortical space by layer-specific horizontal circuits. *Nature* **464**, 1155–1160 (2010)

38. Packer, A. M., Russell, L. E., Dalgleish, H. W. P. & Häusser, M. Simultaneous all-optical manipulation and recording of neural circuit activity with cellular resolution in vivo. Nat. Methods 12, 140–146 (2015)

39. Yang, W., Carrillo-Reid, L., Bando, Y., Peterka, D. S. & Yuste, R. Simultaneous two-photon imaging and two-photon optogenetics of cortical circuits in three dimensions. Elife 7, (2018)

40. Levoy, M., Zhang, Z. & McDowall, I. Recording and controlling the 4D light field in a microscope using microlens arrays. *J. Microsc.* **235**, 144–162 (2009)

41. Prevedel, R. *et al.* Simultaneous whole-animal 3D imaging of neuronal activity using light-field microscopy. *Nat. Methods* **11**, 727–730 (2014)

42. Pégard, N. C. *et al.* Compressive light-field microscopy for 3D neural activity recording. *Optica, OPTICA* **3**, 517–524 (2016)

43. Botcherby, E. J., Juškaitis, R., Booth, M. J. & Wilson, T. An optical technique for remote focusing in microscopy. *Opt. Commun.* **281**, 880–887 (2008)

44. Dalgleish, H. W. *et al.* How many neurons are sufficient for perception of cortical activity? *Elife* **9**, (2020)

45. Dombeck, D. A., Harvey, C. D., Tian, L., Looger, L. L. & Tank, D. W. Functional imaging of hippocampal place cells at cellular resolution during virtual navigation. Nat. Neurosci. 13, 1433–1440 (2010)

46. Marshel, J. H., Kaye, A. P., Nauhaus, I. & Callaway, E. M. Anterior-posterior direction opponency in the superficial mouse lateral geniculate nucleus. Neuron 76, 713–720 (2012)

47. Stamatakis, A. M. et al. Simultaneous Optogenetics and Cellular Resolution Calcium Imaging During Active Behavior Using a Miniaturized Microscope. Front. Neurosci. 12, 496 (2018)

48. Pluta, S. *et al.* A direct translaminar inhibitory circuit tunes cortical output. *Nat. Neurosci.* **18**, 1631–1640 (2015).

44

1004 **Supplementary materials**

1005

1006 **Table 1. Comparison of light-targeting photostimulation methods**

Specific technique	Two-photon optogenetics	One-photon optogenetics			
		Scanning methods (GM & AOD)*	DMD§ projection	CGH**	Our technique 3D-MAP
Pros	• High 3D resolution • High penetration depth • Less cross-talk because of non-linear excitation	• Low power illumination • Compact and inexpensive systems			
		• Reduced cross-talk with sparse excitation	• Fast patterning speed • Large field-of-view	• High 3D resolution	• Large number of DoF • Fast patterning speed • High 3D resolution • Large field-of-view • Less cross-talk from out-of-focus light
Cons	• Small numbers of targets • Small accessible volume	• Rayleigh scattering limits penetration depth • Lower axial resolution than two-photon optogenetics			
	• Small numbers of degrees of freedom • High power illumination (heat and photodamage) • Expensive and sophisticated systems • Slow patterning speed	• No Simultaneous multiple stimulation • Small number of DoF‡	• Low resolution • No depth specificity • 2D modulation • Small number of DoF • Cross-talk from out-of-focus light	• Small number of targets • Small accessible volume • Small number of DoF • Slow patterning speed • Cross-talk from out-of-focus light	• Lossy amplitude modulation that requires bright laser sources.
Refs	[13-19]	[22-24]	[8-12]	[4-7]	This study

1007

1008 * GM: Galvo Mirrors. AOD: Acousto-Optic Deflectors.

1009 ‡ DoF: Degrees of Freedom.

1010 § DMD: Digital Micromirror Device

1011 ** CGH: Computer Generated Holography.

1012

45

1013 **Table 2. Comparison of the cost of one-photon 3D-MAP and two-photon 3D-SHOT[19,24]**

	1P 3D-MAP			2P 3D-SHOT		
Description	Part #	Budget	High performance	Part #	Budget	High performance
Photo-stimulation and imaging lasers	Blue DPSS laser	$700	$9,000	Femtosecond laser for photo-stimulation	$80,000	$160,000
	Yellow DPSS laser	$3,500	$13,000	Femtosecond laser for calcium imaging	$80,000	$140,000
Imaging sensor/system	sCMOS camera	$5,000	$25,000	PMTs and acquisition systems	$20,000	$40,000
Light modulator	DMD and the controller	$2,000	$15,000	LCoS-SLM	$15,000	$60,000
	Scanning mirrors	$2,500	$6,400			
Optical table	min 3'x3'	$4,000	$7,500	min 4'x6'	$8,500	$10,000
Total		$17,700	$75,900		$203,500	$410,000

1014
1015

46

1016
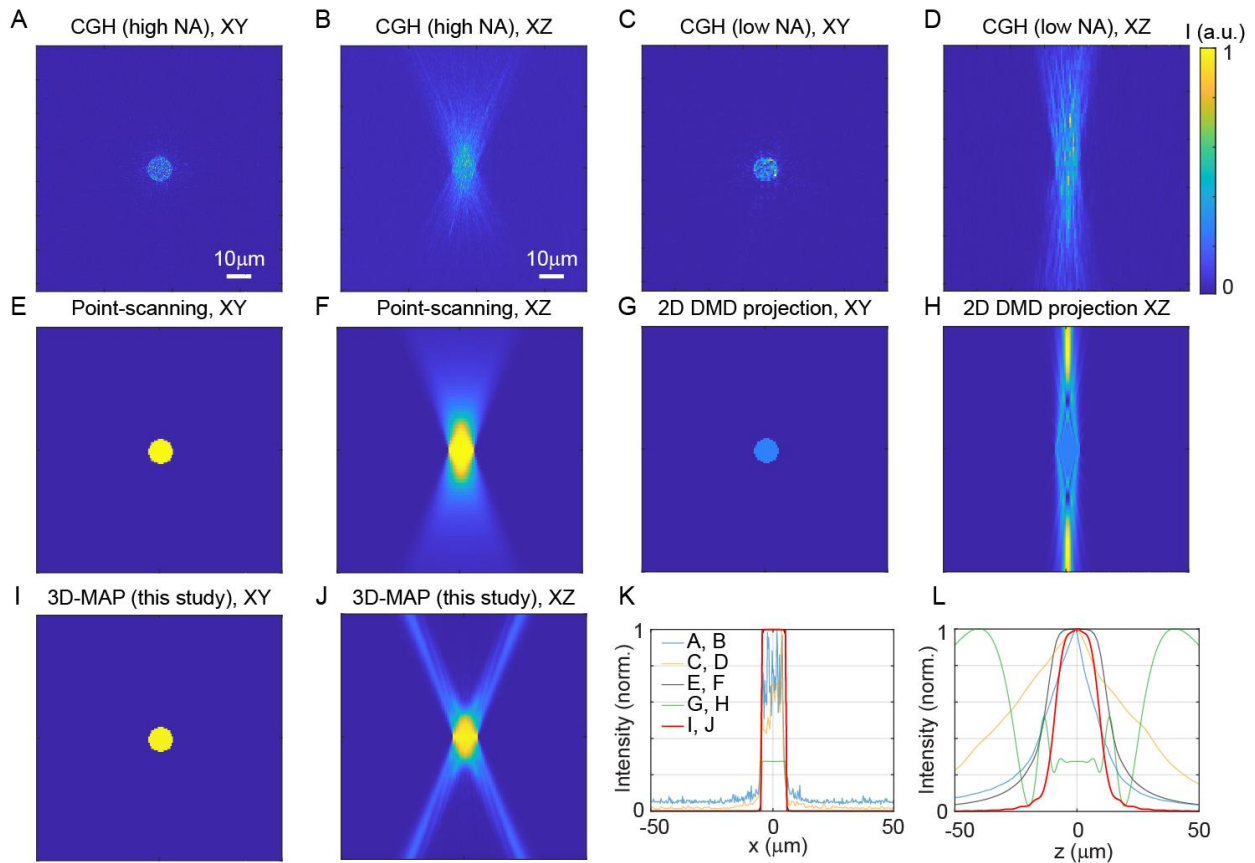
1017

Figure 1—figure supplement 1. Comparison of 3D spatial resolution of 3D-MAP versus existing photostimulation approaches. All simulations aim to generate a 10μm-diameter spot in-focus to match the size of a neuron in order to maximize photostimulation efficiency. The light fields are calculated with 635nm red light illumination and 20x, NA = 1.0 objective lens. The pixel size of the DMD is 7.5μm. The number of pixels of the SLM for CGH is 1152x1152 pixels. (A, B) The lateral cross-section (A) and axial cross-section (B) of CGH at NA = 1.0 (overfill the back aperture). The FOV under high NA illumination is 319x319μm^2, which is much smaller than the FOV of 3D-MAP. (C, D) The lateral cross-section (C) and axial cross-section (D) of CGH at effective NA = 0.55 (under-fill the back aperture) to match the FOV of 3D-MAP (800x800μm^2). (E, F) The lateral cross-section (E) and axial cross-section (F) of spiral scan with a single focus. The

47

1029   total intensity is an incoherent sum of the intensity of each scanning point. (G, H) The

1030   lateral cross-section (G) and axial cross-section (H) of 2D DMD projection. (I, J) The

1031   lateral cross-section (I) and axial cross-section (J) of 3D-MAP (10 overlapping beams).

1032   (K, L) A comparison of intensity profile of all these methods along the x-axis (K) and z-

1033   axis (L). 3D-MAP achieves the highest 3D spatial resolution among all the methods.

1034   Figure (A-J) are in the same size of 100x100μm^2. Scale bar, 10μm.

1035

48

1036
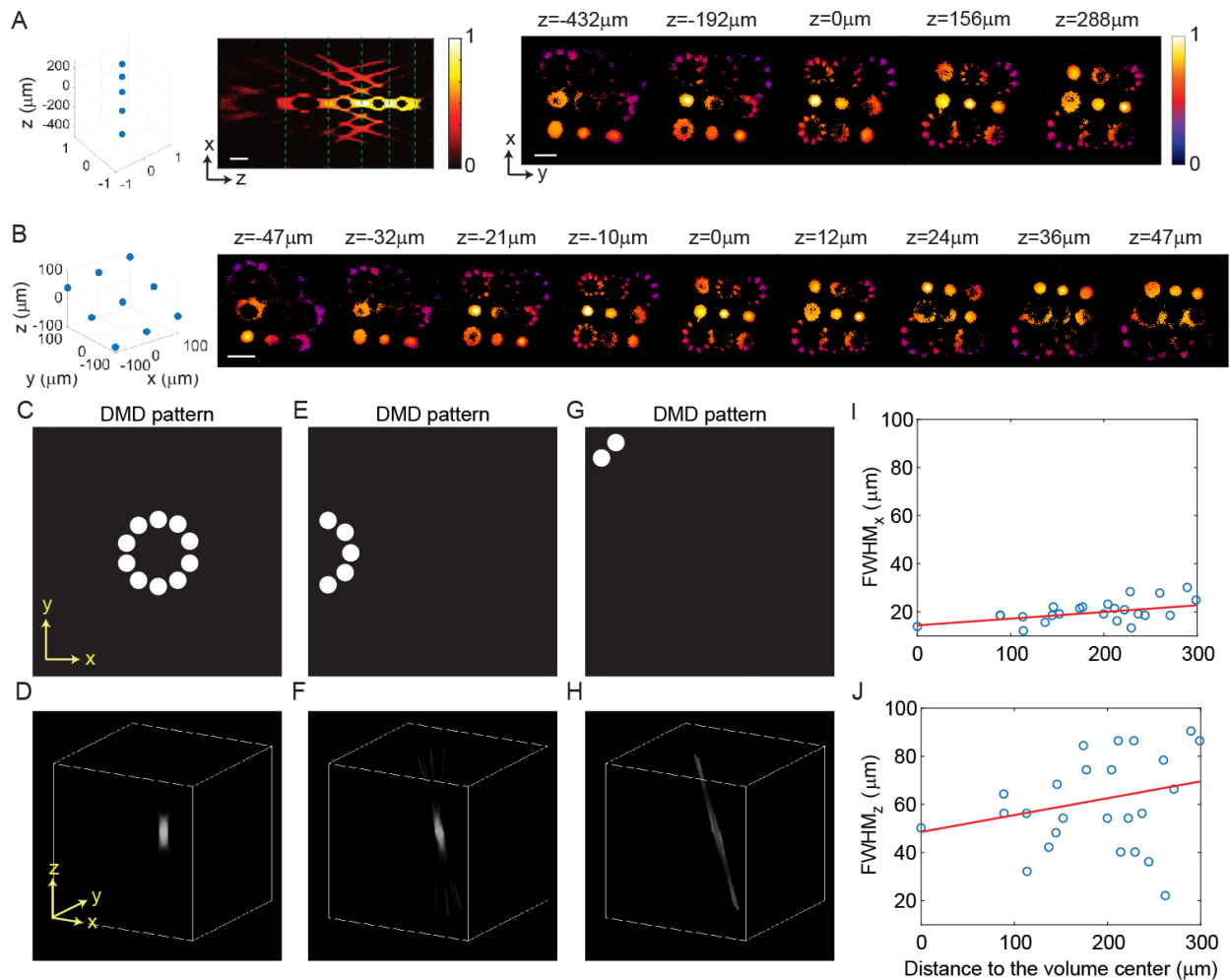
1037
1038

1039 **Figure 2—figure supplement 1. 3D-MAP is able to simultaneously generate multiple**

1040 **foci anywhere in 3D.** (A) Five foci are located right on top of each other along the z-axis.

1041 Left: XZ cross-section. Right: XY cross-section corresponding to the z depths marked

1042 with green dash lines. (B) Nine foci with evenly distributed depths form a tilted plane

1043 across the 3D volume. For both (A) and (B), the target location is indicated in the 3D

1044 diagram on the left, and the corresponding experimental 3D fluorescence measurements

1045 are on the right. The foci are recorded in 3D by capturing a stack of 2D fluorescence

1046 images at various depths of the 3D illumination pattern intercepting a thin, uniform,

1047 fluorescent calibration slide with a sub-stage objective coupled to a camera. Scale bar,

49

1048   100µm. (C-H) Simulation results show spatial resolution degrades near the edge of the

1049   field-of-view. (C) The DMD pattern to generate a focus in the center of the field-of-view.

1050   (D) A focus generated by the 10 beams in c in the center of the accessible volume. (E)

1051   The DMD pattern to generate a focus on the edge of the field-of-view. (F) The focus

1052   generated by the 5 beams in e, which is distorted like a coma aberration. (G) The DMD

1053   pattern to generate a focus in the corner of the field-of-view. (H) The focus generated by

1054   the 2 beams in g, which is severely distorted and barely has any z-sectioning ability. (I-J)

1055   The (I) lateral and (J) axial resolution of the 25 foci showing in Figure 2D versus their

1056   distance to the center of the volume. The blue circles mark the FWHM of the foci, and the

1057   red line is a linear fitting result. On average, the FWHM of the foci 300µm away from the

1058   center is worse than the one in the center, with (I) 63% worse along the x-axis and (J) 38%

1059   worse along the z-axis.

1060

50
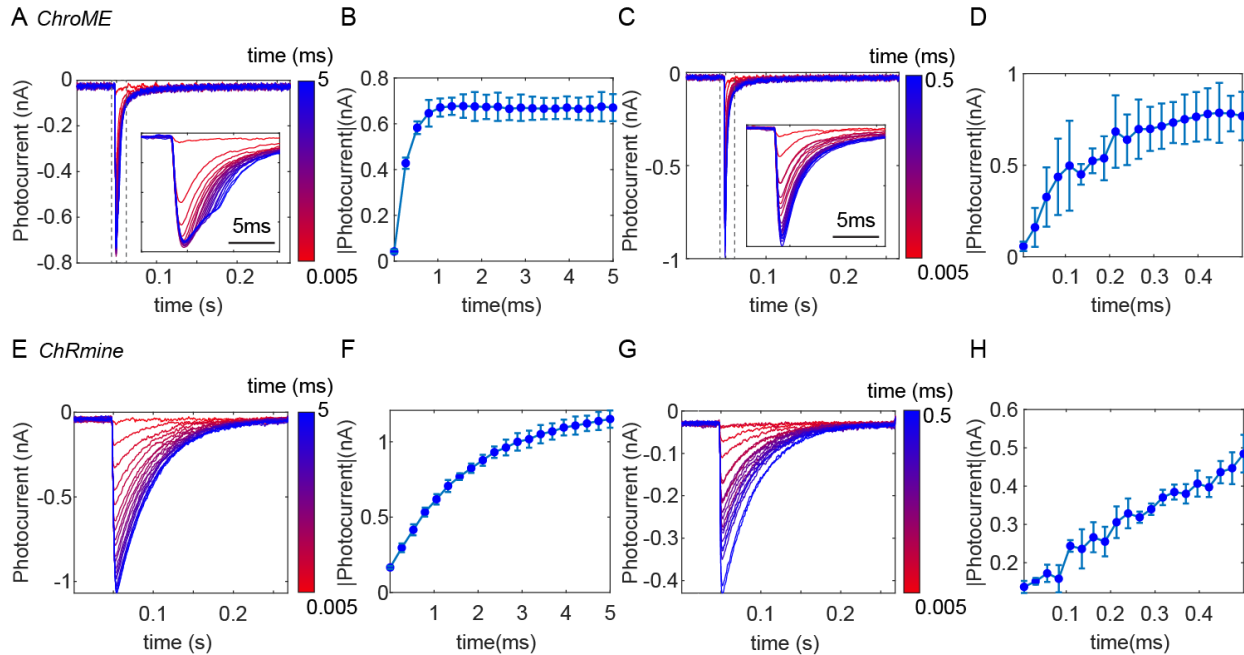
Figure 3—figure supplement 1. Temporal response of (A-D) ChroME and (E-H) ChRmine, expressed in CHO cells. (A, E) Photocurrent measured under various stimulation times (i.e. dwell time) ranging from 5μs to 5ms. We used an acousto-optic deflector (AOD) as a fast shutter to control the stimulation time. Insert plot: the zoom-in view of the photocurrent from 0.045s to 0.06s (dash box). (B, F) The maximum photocurrent at each stimulation time. (C, G) Photocurrent measured at various short stimulation times ranging from 5μs to 500μs. Insert plot: the zoom-in view of the photocurrent from 0.045s to 0.06s (dash box). (D, H) The maximum photocurrent at each short stimulation time. The result shows the photocurrent of opsins linearly increases with the increase of stimulation time, and gradually saturates at longer stimulation time. The saturation stimulation time is about 0.2ms for ChroME and about 2ms for ChRmine. ChroME also has a faster response than ChRmine. Therefore, over kHz patterning speed like what 3D-MAP achieves could reduce the stimulation time so that it becomes possible to photo-stimulate much more sites in the same experimental time.

51
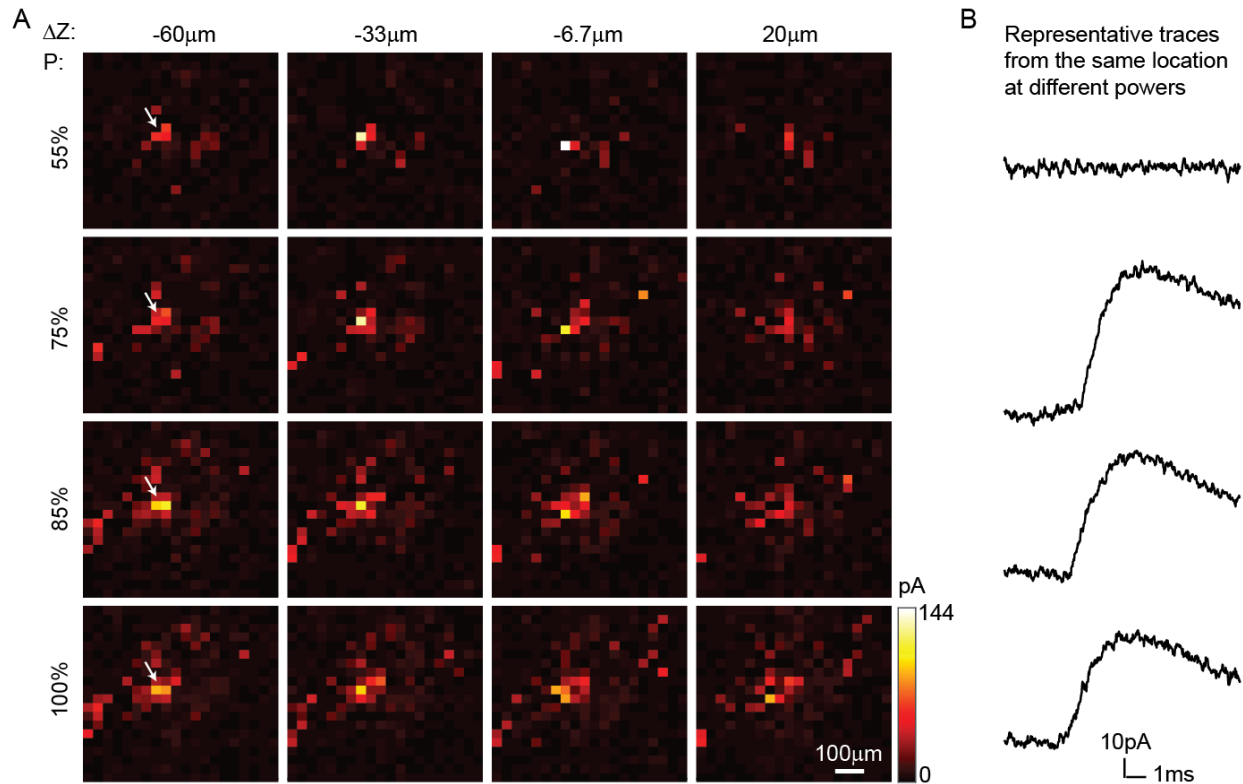
1077
1078

Figure 4—figure supplement 1. 3D-MAP provides mapping of inhibitory synaptic connections *in vivo*. We patched a pyramidal neuron without opsin at [0, 0, 0] and photo-stimulated the volume around it pixel-by-pixel, and the parvalbumin neurons connect to this patched cell via synapses expressed opsin. The current readout reveals the inhibitory synaptic connections from all parvalbumin neurons to this pyramidal neuron. The mapping process is repeated 4 times. (A) Each row of the images is measured under the same stimulation laser power (100% power is 419μW), and each column of the images is at the same axial plane. Scale bar: 100μm. (B) Representative traces of postsynaptic currents under each stimulation power (measured from the pixel pointed by white arrow). These traces elucidate the synaptic connection is binary: once the neuron is photo-stimulated, the synaptic current remains the same, even if the stimulation power is

52

1090   increased. The unique photosensitivity of each neuron helps us to identify different neural

1091   ensembles by changing the stimulation power.

53
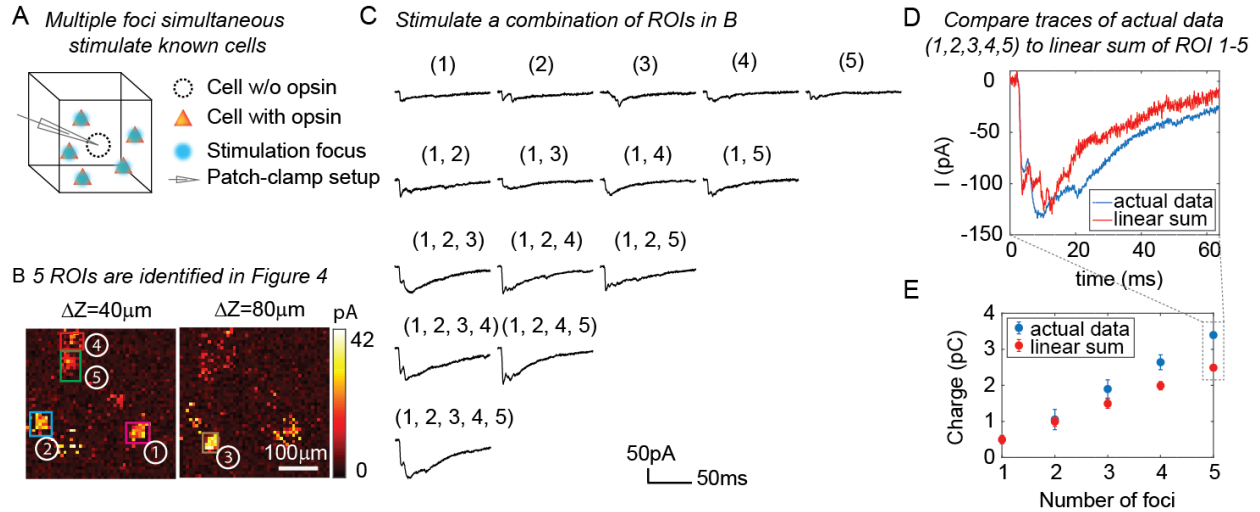
Figure 4—figure supplement 2. 3D-MAP is able to stimulate multiple targets simultaneously to explore network dynamics. (A) Schematic diagram of the experiment. The stimulation ROIs are known to have synaptic connections with the patched interneuron from the widefield mapping as described in Figure 4. (B) The positions of the 5 ROIs are identified in Figure 4E. (C) Representative photocurrent traces for simultaneous stimulation of subsets of the 5 ROIs. Traces are averaged over 4 repetitions. The number(s) above each trace indicate the ROIs that were stimulated to generate the response. (D) Comparison of the actual synaptic response by simultaneous stimulation of ROI 1-5 (blue) to the response calculated by linearly summing the traces when stimulating ROI 1-5 individually (red). The individual response from each ROI is shown in the first row of C. 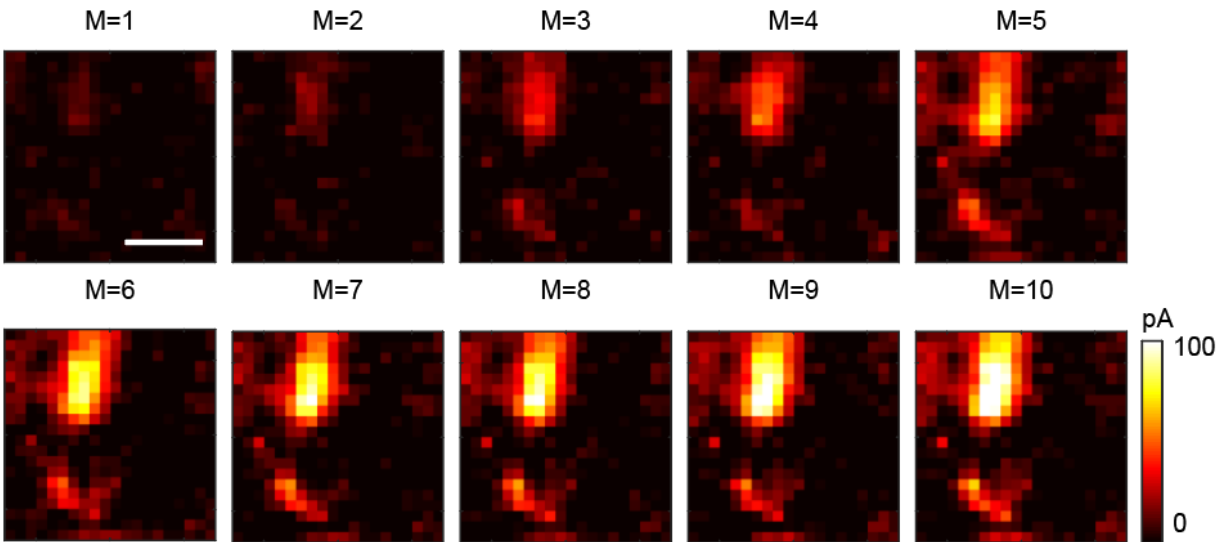(E) Comparison of the integral of the synaptic currents from simultaneous stimulation of multiple connected presynaptic neurons (blue) to the linear sum of the individual stimulation responses (red). The mean and standard deviation of data is calculated from all the k-combinations (number of foci) from the given set of 5 targets. The sample size is $C(5, k), k = 1, 2, 3, 4, 5$.

54

1109

Figure 5—figure supplement 1. Multi-site random simultaneous stimulation by 3D-MAP can reconstruct synaptic connectivity maps with fewer measurements than single-target stimulation. M: number of repeat measurements (see Computational reconstruction framework in Methods). The data is recorded from five simultaneously stimulated foci. The optimization problem is underdetermined for values of M < 5. Assuming the five foci stimulate sites which are sparsely distributed in space, it is possible to reconstruct the synaptic connectivity map with fewer measurements (M=1-4) using compressive sensing. Scale bar, 100µm.

1118
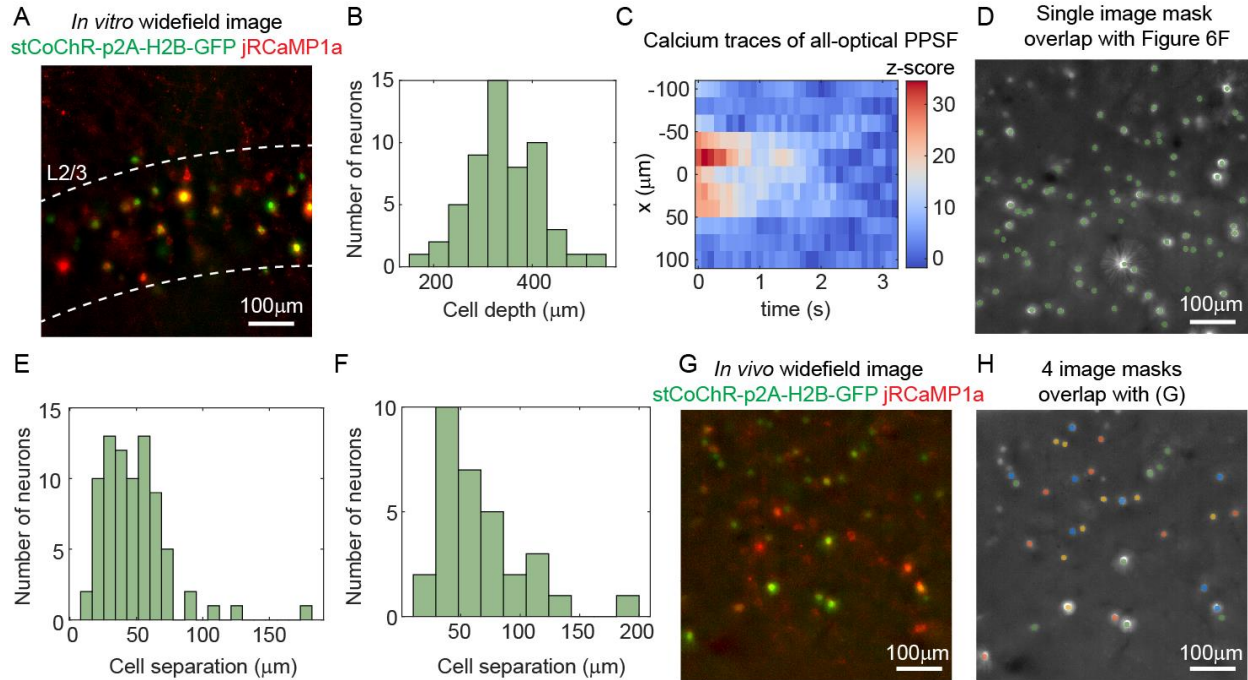
1119

Figure 6—figure supplement 1. All-optical interrogation of neurons with 3D-MAP.

(A) Maximum z projection of the brain slice used in the control experiment (Figure 6B-C).

(B) Histogram of the depth of 55 neurons relative to the surface of the mouse brain. The

expression is in L2/3. (C) An example of calcium traces at 11 lateral locations (y-axis) in

the experiment of *in vivo* all-optical PPSF measurement. The traces are averaged across

10 repetitions of a represented neuron at x=0. (D) The image mask on the DMD for the

80 neurons in the volume shown in Figure 6F. Green, the image mask generated by

image segmentation. Gray scale image, maximum z projection of the widefield image

stack of the somata. (E) Histogram of neuron separation in D. The mean separation of

the 80 neurons is 49±26µm. (F) Histogram of neuron separation in G-H. The mean

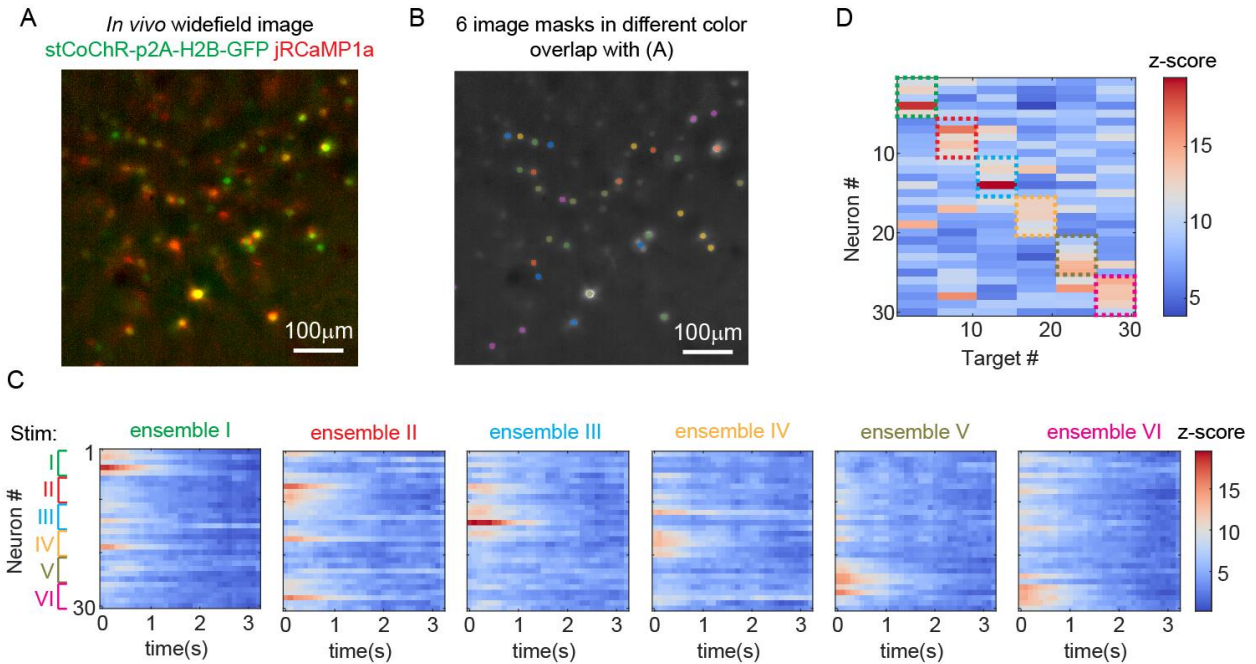separation of the 32 neurons is 67±37µm. (G) Maximum z projection of the *in vivo*

widefield image stack of the neurons in Figure 6H-I. (H) The 4 different image masks for

ensemble stimulation in Figure 6H-I. Neurons labeled by the same color are photo-

stimulated simultaneously. The masks are generated by Poisson disc sampling.

56

1134

1135

Figure 6—figure supplement 2. Another example of stimulating ensembles while imaging all the neurons *in vivo*. (A) Maximum z projection of the *in vivo* widefield image stack of the neurons. (B) 6 distinct patterns for ensemble stimulation and imaging. (C) Calcium activity of 30 neurons that are addressed with the 6 patterns in B. (D) Peak z-score of each calcium trace recorded in c versus the corresponding stimulation patterns. The dashed colored rectangles highlight the neurons that are stimulated in each of the 6 patterns.